

Geochemistry, Geophysics, Geosystems®

RESEARCH ARTICLE

10.1029/2022GC010391

Key Points:

- Both the Tsunakawa-Shaw and the IZZI paleointensity methods give accurate results when applied to aged laboratory thermal remanences
- Introducing alternating-field demagnetization steps into the IZZI method resulted in inaccurate results, as did the multi-specimen protocol
- Low temperature demagnetization (targeting grains with magnetocrystalline anisotropy) is strongly correlated with “fragile” curvature

Supporting Information:

Supporting Information may be found in the online version of this article.

Correspondence to:

Y. Yamamoto,
y.yamamoto@kochi-u.ac.jp

Citation:

Yamamoto, Y., Tauxe, L., Ahn, H., & Santos, C. (2022). Absolute paleointensity experiments on aged thermoremanent magnetization: Assessment of reliability of the Tsunakawa-Shaw and other methods with implications for “fragile” curvature. *Geochemistry, Geophysics, Geosystems*, 23, e2022GC010391. <https://doi.org/10.1029/2022GC010391>

Received 16 FEB 2022
Accepted 14 MAR 2022

© 2022. The Authors.

This is an open access article under the terms of the [Creative Commons Attribution-NonCommercial-NoDerivs License](https://creativecommons.org/licenses/by-nc-nd/4.0/), which permits use and distribution in any medium, provided the original work is properly cited, the use is non-commercial and no modifications or adaptations are made.

Absolute Paleointensity Experiments on Aged Thermoremanent Magnetization: Assessment of Reliability of the Tsunakawa-Shaw and Other Methods With Implications for “Fragile” Curvature

Y. Yamamoto¹ , L. Tauxe² , H. Ahn³, and C. Santos²

¹Kochi University, Kochi, Japan, ²Scripps Institution of Oceanography, La Jolla, CA, USA, ³Korea Institute of Geoscience and Mineral Resources, Daejeon, Republic of Korea

Abstract Absolute paleointensity (API) of the geomagnetic field can be estimated from volcanic rocks by comparing the natural remanent magnetization (NRM) to a laboratory-induced thermoremanent magnetization (Lab-TRM). Plots of NRM unblocking versus Lab-TRM blocking from API experiments often exhibit nonideal curvature, which can result in biased estimates. Previous work showed that curvature can increase with age; however, selection criteria designed to eliminate such behavior yielded accurate estimates for two-year-aged specimens ($70.3 \pm 3.8 \mu\text{T}$; $N = 96$ specimens out of 120 experiments). API can also be estimated in coercivity space. Here, we use the Tsunakawa-Shaw (TS) method applied to 20 specimens aged in the laboratory field of $70.0 \mu\text{T}$ for 4 years, after acquisition of zero-age (fresh) Lab-TRM in the same field. Selection criteria for the TS experiment also yielded accurate results ($68.5 \pm 4.5 \mu\text{T}$; $N = 17$ specimens). In thermal API experiments, curvature is related to internal structure with more single domain-like behavior having the least curvature. Here we show that the fraction of anhysteretic remanent magnetization demagnetized by low-temperature treatment was larger for samples with larger thermal curvatures suggesting a magnetocrystalline anisotropy source. We also tested experimental remedies that have been proposed to improve the accuracy of paleointensity estimates. In particular, we test the efficacy of the multi-specimen approach and a strategy pretreating specimens with low field alternating field demagnetization prior to the paleointensity experiment. Neither yielded accurate results.

Plain Language Summary The strength of the geomagnetic field in the past is a fundamental property of the Earth and volcanic rocks are magnetized as they cool, potentially retaining a record of the ancient field. However, because natural materials were not “designed” to retain records of the field, there are many difficulties in obtaining reliable estimates. Consequently, there are many experimental approaches and methods of analyzing the data. Here, we explore several very different experimental approaches on replicate specimens from a set of samples chosen to represent the range of behaviors observed in lava flows. Specimens were given a fresh magnetization and some were allowed to “age” in a laboratory field for up to 5 years. We find that two methods work quite well while other approaches fail to provide accurate estimates of the field.

1. Introduction

Absolute paleointensity (API) of the geomagnetic field can be estimated from a volcanic rock based on a comparison between a natural remanent magnetization (NRM) with a laboratory induced thermoremanent magnetization (TRM). The comparison can be made by comparing blocking and unblocking temperatures using a Thellier-type experiment (Thellier & Thellier, 1959), the results of which are usually visualized as a so-called Arai plot (Nagata et al., 1963). Arai plots often exhibit curvature, which is regarded as an indication of nonideal behavior (e.g., Dunlop et al., 2005; Dunlop & Özdemir, 2001; Krása et al., 2003; Levi, 1977; Paterson, 2011).

Shaar and Tauxe (2015) investigated curvature over time by applying the IZZI Thellier method of Yu et al. (2004) on specimens whose NRMs resulted in curved Arai plots in the original studies. Laboratory TRMs were given to the specimens by cooling in a field of $70 \mu\text{T}$. The TRMs were then immediately subjected to the IZZI Thellier experiment (“fresh” TRMs). A TRM imparted on sister specimens was set in a laboratory field identical to the original TRM field and allowed to “age” over 2 years, after which they were subjected to the IZZI experiment. Arai plots of the aged specimens were significantly more curved than in the “fresh” TRMs in most cases: the

APIs estimated in the "aged" set of specimens were lower than those in the fresh TRMs and the under-estimate appeared to be related to the degree of curvature in the aged specimens.

In a later study, Santos and Tauxe (2019) imparted laboratory TRMs (70 μT) to many of the same specimens as Shaar and Tauxe (2015), plus an additional set of specimens as they were not curved in the original experiments. Both the initially "curved" and the initially "straight" specimens were subjected to the IZZI experiment. The Arai plots for all the originally curved specimens were significantly straighter than those in the original experiments with some being classified as straight according to the curvature (\vec{k}) criterion of Paterson (2011) and some being somewhat more curved. The accuracy and precision of API estimates was much better in the specimens with "straight" Arai plots. Santos and Tauxe (2019) divided the behaviors of the different specimens into four different categories, that is, straight (original NRM)-straight (fresh TRM) (SS), straight-curved (SC), curved-straight (CS), and curved-curved (CC).

As part of the fresh TRM experiment of Santos and Tauxe (2019), sister specimens were allowed to "age" following the manner of Shaar and Tauxe (2015) with some modifications: in the summer of 2015, the specimens were given fresh TRMs in a laboratory field of 70 μT and placed in controlled fields of either 35 or 70 μT with five orientations (positions 1–5; illustrated in Figure 9 of Tauxe et al., 2021). They conducted IZZI Thellier experiments on the specimens from positions 1, 3, and 5 of the two laboratory fields of 35 and 70 μT after aging for 2 years. When the experimental results were again categorized into straight ($|\vec{k}| \leq 0.164$) or curved ($|\vec{k}| > 0.164$) according to curvatures of the resultant Arai plots, API estimates from total TRMs with the specimens of the laboratory field of 70 μT resulted in an average API of 70 μT for the straight results and 67 μT for the curved results: the former average is accurate while the latter average is slightly low biased. Tauxe et al. (2021) concluded that the curvatures generally increased through time except the specimens of the SS category. They also argued that the curvatures related to the low-biased API estimates resulted from changes in the blocking temperature spectra between fresh TRMs and aged TRMs for the specimens of the CS and CC categories, which were observed to shift to higher unblocking temperatures across the entire temperature range after aging. This they called "fragile" curvature as it seems to disappear in the freshly applied TRMs.

In order to address several major issues associated with "fragile" curvature, Tauxe et al. (2021) also conducted extensive hysteresis measurements including first-order reversal curves (FORCs; Pike et al., 1999) with variants (remFORC, tFORC, and iFORC; Zhao et al., 2017) and IZZI Thellier experiments on sister specimens from the samples studied in Santos and Tauxe (2019). The SS category samples were found to be single domain like, while the others were coarser grained, with the CC category being the coarsest.

There are other ways to estimate API than the IZZI-Thellier approach used by Shaar and Tauxe (2015), Santos and Tauxe (2019), and Tauxe et al. (2021). Some methods attempt to suppress the contribution of coarse grains (multidomain; MD), which have been shown to underestimate the true field intensity (Krása et al., 2003). Others attempt to avoid the effect of chemical alteration that can arise from repeated heating. One approach is to use alternating field demagnetization (AF) as opposed to repeated thermal cycling. The so-called "Shaw" method of Shaw (1974) estimates an API in a coercivity space. This original method was extended by Rolph and Shaw (1985), Tsunakawa and Shaw (1994), Yamamoto et al. (2003), and Mochizuki et al. (2004); the latest version of the Shaw method, formerly called the LTD-DHT Shaw method, is now called the Tsunakawa-Shaw (TS) method (Yamamoto et al., 2015). It is of importance to investigate behavior of "aged" TRMs in a coercivity space in response to the method. In the present study, we applied the TS method to the specimens aged for 4 years in position four of Tauxe et al. (2021).

Another approach proposed to address the problematic behavior of progressive chemical alteration was the so-called multi-specimen protocol (MSP) originally proposed by Hoffman et al. (1989) whereby each specimen was only heated once and only to a moderate temperature (say 400°C). This method was modified by Dekkers and Böhnell (2006) in attempt to also minimize the effect of multidomain grains. The latest modification to the interpretations of the experimental data was proposed by Fabian and Leonhardt (2010). We applied the MSP approach to specimens aged 5 years in position four of the Tauxe et al. (2021) study.

Finally, Dunlop and Özdemir (2001) suggested that subjecting specimens to AF demagnetization during a Thellier-Thellier type experiment could minimize the contribution of MD grains. Here, we incorporate AF demagnetization to 10 mT into a standard IZZI experiment in a protocol we call AF-IZZI. These experiments were carried out on the specimens aged 5 years in position two of Tauxe et al. (2021) study.

2. Methods

For this study, we used the "aged" specimens described by Tauxe et al. (2021). These are rock fragments with a size of a few millimeters, cemented into glass tubes which fit into the sample holders used for ordinary paleomagnetic measurements and experiments in the Scripps Paleomagnetic Laboratory. As we could not measure weights of the fragments precisely, we tentatively treat these as ~10 mg in the present study.

The assumptions laid out by Thellier and Thellier (1959) for paleointensity experiments are based on an expectation that the magnetic particles are single domain (SD), a requirement rarely satisfied in natural samples. Here we test three different approaches to obtaining API estimates from samples that do not satisfy this requirement: The TS method (described in Section 2.1), the MSP method (described in Section 2.2), and the AF-IZZI method (described in Section 2.3). Each of these attempts to correct for bias introduced by nonideal behavior of the specimens.

2.1. TS Method

2.1.1. Background

In the original "Shaw" method (Shaw, 1974) the procedure is as follows:

1. The NRM of a specimen is progressively demagnetized by an AF.
2. An anhysteretic remanent magnetization (ARM) is imparted and subjected to a progressive AF demagnetization (defined as ARM0).
3. The specimen is heated above its Curie temperature to impart a Lab TRM (defined as TRM1).
4. TRM1 is then subjected to a progressive AF demagnetization.
5. An ARM is again imparted and subjected to a progressive AF demagnetization (defined as ARM1).
6. API is estimated from a comparison between NRM and TRM1 from a continuous coercivity interval in which ARM0 is equal to ARM1.

The original method was extended by Rolph and Shaw (1985) to include a correction such that a "corrected" TRM1 is defined as

$$TRM1^* = TRM1 \times \frac{ARM0}{ARM1}$$

Their approach was to estimate an API from a comparison between NRM and TRM1* with a continuous coercivity interval showing a linear relationship. This version was further extended by Tsunakawa and Shaw (1994) to have additional procedures to check the validity of the ARM correction:

1. The specimen is again heated above its Curie temperature to impart a second Lab TRM (defined as TRM2).
2. TRM2 is subjected to a progressive AF demagnetization.
3. An ARM is again imparted and subjected to a progressive AF demagnetization (defined as ARM2).
4. The adjusted TRM2 is defined as

$$TRM2^* = TRM2 \times \frac{ARM1}{ARM2}$$

and the validity is confirmed if TRM1 and TRM2* showed a 1:1 relationship over a certain continuous coercivity interval; this is what is called the double heating test (DHT).

There have been further extensions of the method. The addition of a low-temperature demagnetization step (LTD; Heider et al., 1992; Ozima et al., 1964) prior to each progressive AF demagnetization is intended to remove the contribution of multi domain (MD)-like remanences (Yamamoto et al., 2003). Heating the specimen in a vacuum (~1–10 Pa) is meant to suppress thermal alteration when imparting a Lab TRM (Mochizuki et al., 2004). The latest version of the Shaw method includes all these modifications. This was called the LTD-DHT Shaw method and is now called the Tsunakawa-Shaw (TS) method (Yamamoto et al., 2015). Note that there has been an attempt to incorporate the microwave excitation technique into the LTD-DHT Shaw method in lieu of conventional heating (Yamamoto & Shaw, 2008).

Since the 2000s, validity of the TS method has been assessed by historical lavas in Hawaii (Yamamoto et al., 2003) and Japan (Mochizuki et al., 2004; Oishi et al., 2005; Yamamoto & Hoshi, 2008), and by simulated archeological materials in Japan (Yamamoto et al., 2015). In the course of these assessments, it has been pointed out that the ARM correction is effective not only for correcting thermal alterations but also for correcting remanence anisotropy and compensating for possible magnetostatic interactions among magnetic domains. With this as background, the TS method has been applied to old igneous rocks in Africa (Ahn et al., 2016; Yoshimura et al., 2020), China (Yamamoto, Tsunakawa, et al., 2007), French Polynesia (Mochizuki et al., 2011; Yamamoto, Ishizuka, et al., 2007; Yamamoto & Tsunakawa, 2005), Hawaii (Singer et al., 2019; Yamamoto & Yamaoka, 2018), Japan (Kato et al., 2018; Mochizuki et al., 2013; Okayama et al., 2019; Tsunakawa et al., 2009; Yamamoto et al., 2010), Korea (Ahn & Yamamoto, 2019), Louisville seamount (Yamazaki & Yamamoto, 2014), New Zealand (Mochizuki et al., 2006), and archeological materials in Japan (Kitahara et al., 2018, 2021). Although LTD treatments are not necessarily included, the TS method has also been applied to Precambrian rocks (Lloyd, Biggin, et al., 2021; Thallner, Biggin, & Halls, 2021; Thallner, Biggin, McCausland, & Fu, 2021), partly with consideration for different sets of selection criteria (Lloyd, Paterson, et al., 2021). It has also been shown that the APIs determined by the TS method are linearly related to the sedimentary paleointensities of the last 1.5–2 million years (Mochizuki et al., 2021).

2.1.2. Experiment

Among the "aged" specimens in Tauxe et al. (2021), 20 specimens from position 4, aged in a laboratory field of 70 μ T were used in the present study for the TS method. They consisted of six specimens from the SS category, four specimens from the SC category, six specimens from the CS category, and four specimens from the CC category.

Paleointensity experiments using the TS method were conducted according to the procedures explained in detail in Yamamoto and Tsunakawa (2005), except that the progressive demagnetizations for ARM00, ARM10, and ARM20 were not included. Experimental conditions were as follows, and a experimental result is usually represented as in Figure 1.

1. Progressive AF demagnetizations were conducted at 2–20 mT steps from 0 mT (H_0) up to 180 mT (H_{\max}), using an AF tumbling demagnetizer (Natsuhara Giken, DEM-95C), see inset to Figure 1a. Measurements of remanences were carried out after each AF demagnetization step using a superconducting rock magnetometer (SRM) (2G Enterprises Model 755–4.2 cm).
2. Lab TRMs were imparted by heating the specimens in a vacuum (\sim 1–10 Pa) to a maximum temperature of 610°C, which was held for 10 (20) min during the first (second) heating, in a laboratory field of 60 μ T using a thermal demagnetizer/remagnetizer (Natsuhara Giken, TDS-1). The field was applied to the cylindrical axis of the glass tube containing the specimen. The entire heating and cooling cycle took about 3 hr.
3. ARMs were imparted by a direct current bias field of 50 μ T with a maximum AF of 180 mT (H_{\max}), toward directions approximately parallel to the NRM and Lab TRMs of each specimen.
4. LTD was conducted such that the specimens were soaked in a nonmagnetic dewar filled with liquid nitrogen for 2 min and taken out from the dewar, left at room temperature for 30 min. The complete cooling/warming cycle was carried out in zero field.

To estimate APIs, we developed a Python code to analyze a series of remanence data obtained by the experiments. The development was benefitted from a series of standard functions in PmagPy (Tauxe et al., 2016) and has been added to that software package. Analytical procedures are as follows.

1. Finding a coercivity interval H_1 – H_2 giving the characteristic component of NRM in the orthogonal plot of AF demagnetization (e.g., black dots in inset to Figure 1a).
2. Calculating parameters on all possible continuous coercivity intervals within H_1 – H_{\max} for an NRM-TRM1* plot as shown in Figure 1a and H_0 – H_{\max} for a TRM1-TRM2* plot, as in Figure 1d. The intervals are defined by at least 4 data points ($N \geq 4$). The parameters include fractions of an NRM (f_N) and a TRM1 (f_T) adopted for linear segments, and slopes and correlation coefficients of the segments in an NRM-TRM1* plot (slope_N , r_N) and a TRM1-TRM2* plot (slope_T , r_T).
3. Combining the calculated parameters for an NRM-TRM1* plot and a TRM1-TRM2* plot, such that the continuous coercivity interval adopted in an NRM-TRM1* plot is included in that adopted in a TRM1-TRM2*

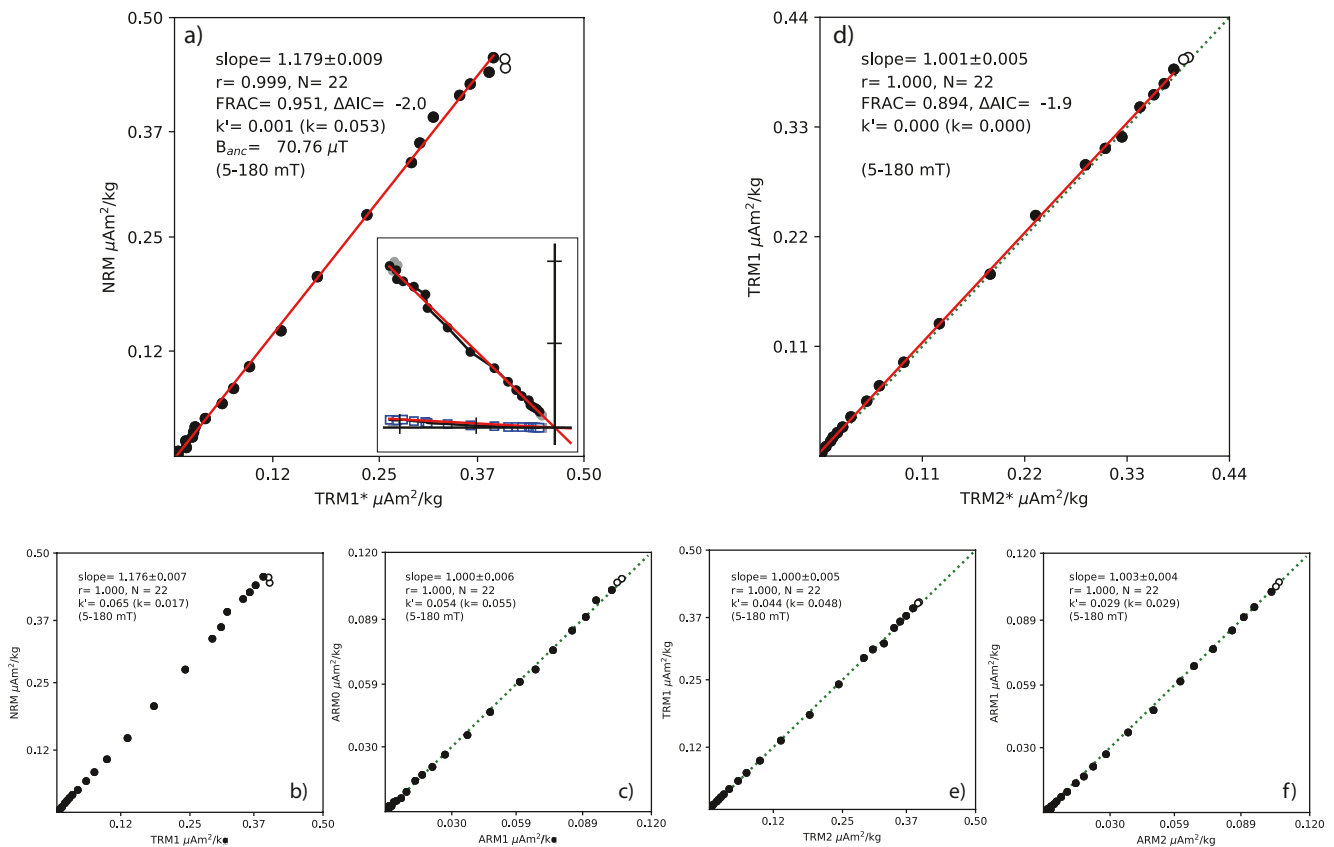


Figure 1. A representative successful result by the Tsunakawa-Shaw (TS) method for a specimen of the straight-straight (SS) category, mc120c. (a–c) Results from the first laboratory heating, where closed symbols indicate coercivity intervals for the linear segments. Alternating field (AF) demagnetization results on the natural remanent magnetization (NRM) are also shown as an inset of an orthogonal vector-end-point diagrams, where closed (open) symbols indicate projections onto horizontal (vertical) planes. (d–f) Results from the second laboratory heading.

plot (minimum (maximum) coercivity of the linear segment in a TRM1-TRM2* is not higher (lower) than that in a NRM-TRM1* plot). A list of the combinations is obtained.

4. Applying selection criteria to the list to screen out the combinations not fulfilling the criteria. The criteria are as follows, which are applied step by step in the following order: $f_T \geq 0.15$; $r_T \geq 0.995$; $0.95 \leq \text{slope}_T \leq 1.05$; $f_N \geq 0.15$; $r_N \geq 0.995$. These are mostly equivalent to those first defined in Yamamoto et al. (2003). If no combinations remained after a certain step, the application is abandoned just before that step.
5. Sorting the screened combinations by a fraction of NRM (f_N) and selecting a combination with the largest fraction: it gives a sole solution for an API estimate. The solution provides a series of biplots, that is, NRM-TRM1* (Figure 1a), NRM-TRM1 (Figure 1b), ARM0-ARM1 (Figure 1c), TRM1-TRM2* (Figure 1d), TRM1-TRM2 (Figure 1e), and ARM1-ARM2 (Figure 1f) plots. To characterize curvatures in the biplots, the \bar{k} statistic of Paterson (2011) was applied to calculate $|\bar{k}|$ and the modified version $|\bar{k}'|$ of Paterson et al. (2014) for reference.

2.2. MSP Method

A companion set of specimens, aged in a 35 μT field applied at an angle of 45° to the TRM (position two described by Tauxe et al., 2021) were subjected to the multi-specimen experiment (MSP) of Dekkers and Böhnel (2006) as modified by Fabian and Leonhardt (2010). The specimens were split into four groups, each containing one or more specimens from the four categories (SS, SC, CS, and CC). We followed these steps:

1. M0: The NRM (in this case, the aged TRM) was measured for all specimens.

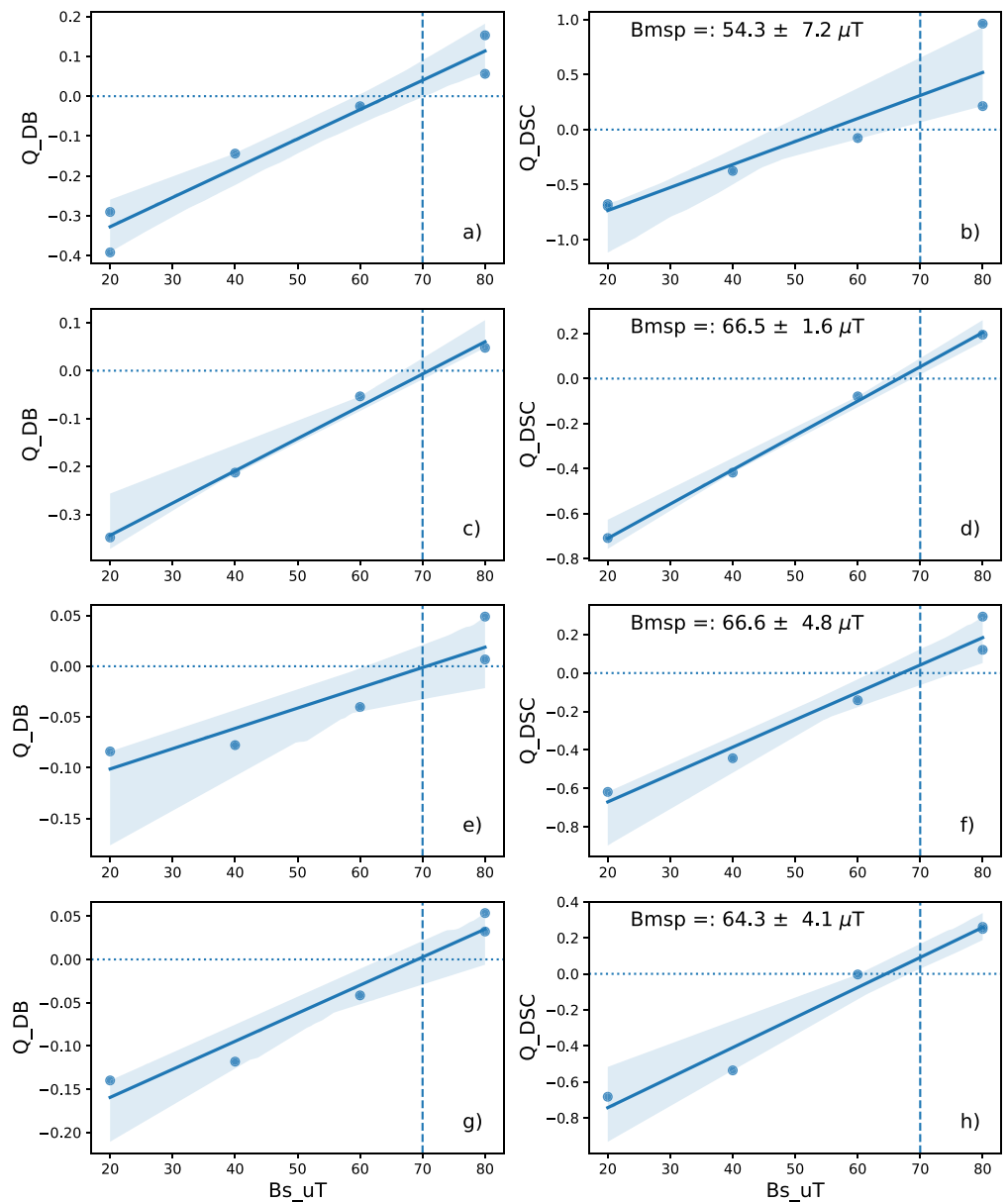


Figure 2. Multi-specimen protocol (MSP) experiment performed on specimens from the four groups of samples. Left-hand panel is Q_{DB} (Dekkers & Böhnel, 2006) against laboratory field (in μT) and right-hand panel is Q_{DSC} (Fabian & Leonhardt, 2010) plotted against laboratory field. B_{msp} is the estimated API along with the two standard deviations. The vertical dashed lines are the actual field in which the samples were cooled prior to aging. (a–b) Straight-straight (SS) category. (c–d) Straight-curved (SC) category. (e–f) Curved-straight (CS) category. (g–h) Curved-curved (CC) category.

2. M1: At least one specimen from each category (SS, SC, CS, and CC) was given a partial TRM (pTRM) in one of four fields (20, 40, 60, or 80 μT). The pTRMs were applied parallel to the NRM direction at a temperature of 450°C.
3. M2: Same as M1 but in a field antiparallel to the NRM.
4. M3: Heating to 450°C in zero field, then cooling in a field parallel to the NRM.
5. M4: Repeat of M1.

In the original MSP method of Dekkers and Böhnel (2006), the parameter Q_{DB} (left-hand panels in Figure 2) is calculated as $(M1 - M0)/M0$ and plotted against the field applied for each group. For the modification proposed

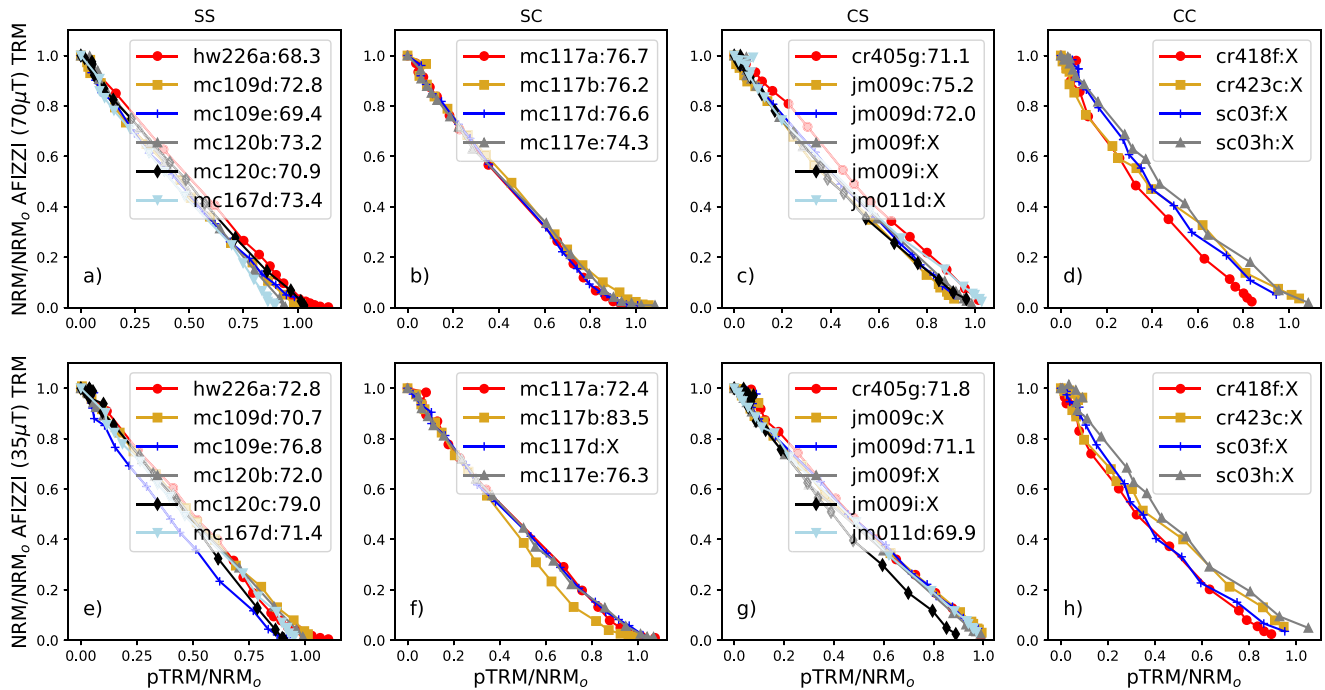


Figure 3. Arai diagrams for all the results of the AF-IZZI experiment. Specimens in the top (bottom) panel were aged in a 70 μT (35 μT) field. The four vertical panels are straight-straight (SS), straight-curved (SC), curved-straight (CS), and curved-curved (CC) results. The legends in each subplot have the sample names and the API estimated by CCRIT. Values listed as "X" are specimens that failed the CCRIT criteria.

by Fabian and Leonhardt (2010), Q_{DSC} is calculated as $2((1 + \alpha)M1 - M0 - \alpha M3)/(2M0 - M1 - M2)$, where α is 0.5. Q_{DSC} is plotted on the right-hand panels in Figure 2. The best-fit lines and standard deviations are calculated with the Python `scipy.stats.linregress()` function.

2.3. AF-IZZI Method

Dunlop and Özdemir (2001) suggested that it might be advantageous to demagnetize the NRM by using AF demagnetization in a 10 mT field. The rationale was to demagnetize the low stability (assumed to be multi-domain) grains and isolate the high stability (single domain) grains. We tested this method on a set of sister specimens to the two other experiments. These were the 24 specimens that were aged for 5 years in 35 and 70 μT fields in position two of Tauxe et al. (2021) study. In our experiments, each specimen was subjected to a 10 mT AF demagnetization step prior to measurement in the standard IZZI experimental protocol of Yu et al. (2004). Arai plots for these experiments are shown in Figure 3.

Table 1
Specimen Level CCRIT (Cromwell et al., 2015) Selection Criteria

n	DANG	MAD	β	SCAT	FRAC	g_{\max}	$ \vec{k} $
4	$\leq 10^\circ$	$\leq 5^\circ$	0.1	TRUE	0.78	≥ 0.6	0.164

Note. For definitions, see Paterson et al. (2014). n : minimum number of consecutive demagnetization steps, DANG: deviation angle, MAD: maximum angle of deviation, β : the maximum ratio of the standard error to the best fit slope, SCAT: a Boolean value that indicates whether the data fall within 2σ bounds of the best-fit slope, FRAC: fractional remanence, g_{\max} : maximum fractional remanence removed between consecutive temperature steps, and $|\vec{k}|$: maximum curvature.

To calculate API, we applied the CCRIT selection criteria of Cromwell et al. (2015) and Tauxe et al. (2016). These are listed in Table 1 and are designed to screen out data effected by nonideal particles, such as alteration of the magnetization due to heating and nonlinear behavior on the Arai plots. In particular, the latter eliminates specimens with $|\vec{k}|$ values in excess of 0.164, as recommended by Paterson (2011). For this, we used the program `Thellier_GUI` (Shaar & Tauxe, 2013), which finds the API at a specimen level that passes the CCRIT criteria and yields the tightest distribution of API at a "site". Here, we take the category as the "site". We calculate the average API as the average of all selected specimen values along with the standard deviation.

Table 2
Summary of Results From the TS Experiments

Sample	CAT	LTD	API	H _{1N}	H _{2N}	Slope _N	f _N	r _N	k'	k' _{NRM-TRM1}	k' _{ARM0-ARM1}	H _{1T}	H _{2T}	slope _T	f _T	r _T
mc167d	SS	2.1	71.0	0	180	1.18	1.00	0.999	0.070	0.101	0.000	0	180	1.01	1.00	1.00
mc120c	SS	3.2	70.8	5	180	1.18	0.951	0.999	0.001	0.0174	0.0551	5	180	1.00	0.894	1.00
mc120b	SS	2.9	67.7	35	140	1.13	0.519	0.997	0.144	0.0915	0.0948	35	140	1.05	0.555	0.998
mc109d	SS	6.9	71.7	10	180	1.20	0.679	1.00	0.051	0.121	0.0734	8	180	0.961	0.842	1.00
mc109e	SS	8.3	66.3	5	160	1.11	0.873	0.999	0.043	0.000	0.00332	0	160	1.05	0.992	1.00
hw226a	SS	5.3		18	180	0.742	0.611	0.910	0.627	0.242	0.0103	0	180	0.967	1.00	0.967
mc117b	SC	3.7	70.1	8	180	1.17	0.821	1.00	0.058	0.0273	0.0346	2	180	0.986	0.901	1.00
mc117d	SC	6.4	69.0	18	180	1.15	0.488	0.999	0.030	0.0848	0.000	12	180	0.969	0.737	1.00
mc117e	SC	7.5	70.4	5	180	1.17	0.850	1.00	0.000	0.134	0.0961	0	180	1.02	1.00	1.00
mc117a	SC	3.8	67.3	8	180	1.12	0.774	0.998	0.142	0.185	0.00204	2	180	0.989	0.476	1.00
jm009c	CS	11.6	74.3	15	90	1.24	0.633	0.998	0.073	0.148	0.288	0	90	0.986	0.860	0.999
jm009d	CS	5.3	70.6	12	180	1.18	0.740	0.997	0.175	0.402	0.559	0	180	1.04	1.00	1.00
jm011d	CS	9.6	67.5	8	180	1.13	0.826	0.999	0.010	0.0586	0.0714	5	180	0.997	0.908	1.00
jm009i	CS	7.7	68.2	10	180	1.14	0.817	1.00	0.015	0.311	0.282	8	180	1.00	0.893	0.999
jm009f	CS	10.1	73.4	18	180	1.22	0.691	0.999	0.000	0.0627	0.145	18	180	0.984	0.698	0.998
cr405g	CS	7.8	64.3	8	180	1.07	0.881	0.998	0.165	0.934	0.875	0	180	0.998	1.00	1.00
cr418f	CC	18.5	67.0	5	20	1.12	0.450	0.999	0.116	0.0866	0.0498	5	20	0.951	0.445	0.998
cr423c	CC	14.7	54.2	5	70	0.904	0.813	0.995	0.126	0.287	0.0215	5	70	0.973	0.836	0.997
sc03f	CC	14.3		15	180	1.26	0.722	0.984	0.407	0.775	0.979	0	180	1.03	1.00	0.998
sc03h	CC	10.0		40	180	1.28	0.281	0.973	0.000	0.288	0.243	20	180	1.00	0.761	0.995

Note. CAT: category; LTD: fraction lost in ARM0 on LTD in percent; API: estimated absolute paleointensity in μT ; H_{1N}, H_{2N}: minimum and maximum AF field (in mT) taken for the linear segment in the NRM-TRM1* plot; Slope_N, Slope_T: slopes of the linear segments in the NRM-TRM1* and TRM1-TRM2* plots; f_N, f_T: NRM and TRM1 fractions of the linear NRM-TRM1* and TRM1-TRM2* segments; r_N, r_T: correlation coefficients of the linear NRM-TRM1* and TRM1-TRM2* segments; |k'|: curvatures of the linear NRM-TRM1* segments; |k'|_{NRM-TRM1}, |k'|_{ARM0-ARM1}: curvatures in the NRM-TRM1 and ARM0-ARM1 plots; H_{1T}, H_{2T}: minimum and maximum AF field (in mT) taken for the linear segment in the TRM-TRM2* plot. Numbers in italics are out of the selection criteria.

2.4. Reanalysis of Published IZZI Thellier Results Using CCRIT

In addition to the AF-IZZI results presented here, we applied the CCRIT criteria to the results published earlier by Santos and Tauxe (2019) and Tauxe et al. (2021) on fresh or aged TRMs given to sister specimens of those considered in this paper. There were a total of 24 specimens in the first study and 120 specimens (positions 1, 3 and 5) in the second study. Experimental details are given in the original references.

3. Results

The TS results are listed in Table 2; those for the MSP experiments are listed in Table 3; AF-IZZI results are in Table 4. Our reanalysis of the IZZI Thellier results of Santos and Tauxe (2019) and Tauxe et al. (2021) using the CCRIT criteria are listed in Tables 5 and 6, respectively. A summary of all results from our experiments are shown in Figure 4.

3.1. TS Method

A total of 17 API estimates by the TS method were successfully obtained by the analysis described in Section 2. It resulted in an overall average (median) of 68.5 (69.0) μT with a standard deviation of 4.5 μT , indistinguishable from the laboratory field of 70 μT used for acquisition of the fresh TRMs. Representative results from each category are illustrated in Figure 1 and Figures

Table 3
Results of the Multi-specimen (MSP) Experiments Described in Section 2.2

CAT	API	1 σ	N	Std err
SS	54.3	3.6	6	5.2
SC	66.5	0.8	4	0.8
CS	66.6	2.4	5	3.0
CC	64.3	2.0	5	2.6

Note. CAT: category; API: estimated absolute paleointensity in μT ; 1 σ : one standard deviation uncertainty; N: number of specimens in the category. Std Err: standard error of the estimate.

Table 4
Results From the AF-IZZI Experiment, Analyzed With the CCRIT Selection Criteria of Cromwell et al. (2015); Tauxe et al. (2016)

Specimen	CAT	API	β	FRAC	g_{\max}	$ \vec{k} $	SCAT	DANG	MAD
mc109e-SB2	SS	76.8	0.02	0.79	0.15	0.1566	True	1.13	1.94
mc109e-SA2	SS	69.4	0.02	0.80	0.14	0.1464	True	3.83	2.05
mc109d-SB2	SS	70.7	0.01	0.80	0.15	0.0814	True	2.78	2.29
mc109d-SA2	SS	73.1	0.02	0.88	0.15	0.1483	True	1.49	2.25
hw226a-SB2	SS	72.8	0.02	0.97	0.16	0.0000	True	1.13	1.92
hw226a-SA2	SS	68.3	0.01	0.80	0.28	0.0000	True	1.55	1.39
mc120b-SA2	SS	73.2	0.00	0.81	0.17	0.0171	True	0.97	4.86
mc120b-SB2	SS	72.0	0.01	0.86	0.16	0.0794	True	0.68	3.00
mc120c-SA2	SS	70.9	0.02	0.87	0.18	0.0913	True	2.57	4.61
mc120c-SB2	SS	79.0	0.01	0.84	0.26	0.0000	True	0.83	1.41
mc167d2-SA2	SS	73.4	0.01	0.79	0.21	0.0322	True	2.37	2.73
mc167d2-SB2	SS	71.4	0.01	0.99	0.21	0.0526	True	1.86	2.88
mc117e-SB2	SC	76.3	0.02	0.79	0.15	0.1254	True	2.73	4.38
mc117e-SA2	SC	74.3	0.02	0.93	0.30	0.1517	True	1.46	2.80
mc117d-SA2	SC	76.6	0.01	0.80	0.30	0.0345	True	1.29	1.56
mc117b-SB2	SC	83.5	0.02	0.92	0.19	0.1460	True	2.24	3.45
mc117b-SA2	SC	76.2	0.02	0.83	0.24	0.1077	True	0.60	2.16
mc117a-SB2	SC	72.4	0.02	0.86	0.35	0.1419	True	1.17	1.58
mc117a-SA2	SC	76.7	0.01	0.94	0.29	0.1489	True	0.76	2.90
cr405g1-CA2	CS	71.1	0.01	0.82	0.17	0.0000	True	1.84	4.92
cr405g1-CB2	CS	73.3	0.02	0.90	0.16	0.1373	True	2.05	4.82
jm009c1-CA2	CS	75.2	0.02	0.82	0.24	0.1618	True	2.92	4.49
jm009d1-CA2	CS	72.5	0.01	0.81	0.21	0.0903	True	5.86	2.22
jm009d1-CB2	CS	73.2	0.02	0.84	0.18	0.1593	True	3.72	3.73
jm011d1-CB2	CS	69.9	0.02	0.83	0.26	0.1627	True	4.62	3.99

Note. CAT: category; API: estimated absolute paleointensity in μT . Other parameters are as in Table 1.

S1–S3 of Supporting Information S1. Details of the results are listed in Table 2 and in Figure S4 of Supporting Information S1.

There are five API estimates from the SS category, four from the SC category, six from the CS category, and two from the CC category (Figure S4a in Supporting Information S1). They are derived from 45% to 100% fraction of the total NRM (Figure S4b in Supporting Information S1). At the category level, an average (median) and a standard deviation of the API estimates are as follows: $69.5 (70.8) \pm 2.4 \mu\text{T}$ for SS; $69.2 (69.6) \pm 1.4 \mu\text{T}$ for SC; $69.7 (69.4) \pm 3.8 \mu\text{T}$ for CS; and $60.6 (60.6) \pm 9.1 \mu\text{T}$ for CC. Within the 95% confidence limits (2σ), there are no significant differences in average/median APIs across the categories. Among the API specimen level estimates, the estimate of $54.2 \mu\text{T}$ from the CC category specimen cr423c is significantly different from the other 16 estimates. If we excluded it as an outlier, there is only one specimen (cr418f) for the CC group, with an API estimate of $67.0 \mu\text{T}$. However, we do not feel justified in subjective exclusion of results and regard the TS method as applied to the CC group as inconclusive.

Variable fractions of the remanences were erased by LTD during the course of the paleointensity experiments. At the category level, an average of LT-demagnetized ARM0 fractions are as follows: $4.8 \pm 2.5\%$ for SS ($N = 6$); $5.4 \pm 1.9\%$ for SC ($N = 4$); $8.7 \pm 2.2\%$ for CS ($N = 6$); and $14.4 \pm 3.5\%$ for CC ($N = 4$) (Figure S4c in Supporting Information S1 and Table 2). It is clear that the demagnetized fractions are larger in the CS and CC categories than those in the SS and SC categories. Degrees of the LT-demagnetized ARM0 fractions are independent of the

Table 5
Data From Santos and Tauxe (2019) Reanalyzed Using the CCRIT Specimen Level Criteria

Specimen	CAT	API	β	FRAC	g_{\max}	$ \vec{k}' $	SCAT	DANG	MAD
mc109d-SZb	SS	71.3	0.00	0.97	0.12	0.0391	True	0.67	0.55
hw226a-SZb	SS	71.0	0.01	0.79	0.18	0.0642	True	1.97	2.29
mc120b-SZb	SS	72.3	0.01	0.78	0.21	0.0000	True	0.61	1.11
mc120c-SZb	SS	70.8	0.00	1.00	0.13	0.0029	True	1.47	2.48
mc167d2-SZb	SS	71.2	0.01	0.82	0.19	0.0470	True	1.14	4.35
mc109e-SZb	SS	71.4	0.01	0.87	0.18	0.0962	True	0.64	0.57
mc117d-SZb	SC	72.8	0.02	0.81	0.27	0.0000	True	0.70	1.41
mc117e-SZb	SC	72.8	0.01	0.86	0.23	0.0852	True	0.54	0.66
mc117a-SZb	SC	72.8	0.01	0.88	0.20	0.0000	True	0.46	0.41
mc117b-SZb	SC	72.8	0.02	0.90	0.12	0.1326	True	0.92	0.78
jm011d1-CZb	CS	71.2	0.02	0.91	0.20	0.1537	True	0.84	1.02
jm009i2-CZb	CS	78.5	0.02	0.79	0.15	0.1007	True	1.76	0.42
cr405g1-CZb	CS	70.3	0.01	0.84	0.10	0.0507	True	0.34	0.80
jm009d1-CZb	CS	72.6	0.01	0.80	0.20	0.0043	True	1.17	0.28
jm009c1-CZb	CS	70.4	0.02	0.87	0.31	0.1537	True	1.25	1.32
jm009f2-CZb	CS	67.8	0.02	0.88	0.33	0.1343	True	0.87	0.79
sc03f-CZb	CC	80.5	0.02	0.79	0.10	0.1202	True	1.36	2.06
cr418f-CZb	CC	70.3	0.02	0.79	0.21	0.1470	True	0.89	0.69

Note. Specimen: specimen name; CAT: category assigned by Tauxe et al. (2021) and used in this paper; API: absolute paleointensity estimate in μT ; β , FRAC, g_{\max} , $|\vec{k}'|$, SCAT, DANG, and MAD are the parameters used in CCRIT to estimate API. See Paterson et al. (2014) for definitions and Table 1 for threshold values.

curvatures ($|\vec{k}'|$) in the NRM-TRM1 plots (Figure 5a) and the ARM0-ARM1 plots (Figure 5b), which were solely based on post-LTD remanences, across the categories. Curvatures were observed in the NRM-TRM1 plots and the ARM0-ARM1 plots even after LTD and they were larger in the CS and CC categories than those in the SS and SC categories (Figure S4d and S4e in Supporting Information S1). However, the degree of curvatures in the two plots are similar across the categories (Figure 5c) resulting in more or less straight NRM-TRM1* plots with reasonable API estimates except one (54.2 μT) from the specimen cr423c.

All the 17 successful results were accompanied by $|\vec{k}'|$ values not more than 0.2 for the NRM-TRM1* diagrams (Table 2). A criterion of $|\vec{k}'| \leq 0.2$ has been suggested as an alternative selection criterion in the Shaw-type method (Lloyd, Paterson, et al., 2021). They argued that the ARM correction might occasionally fail resulting in inaccurate API estimate, if $|\vec{k}'| > 0.1$ for an NRM-TRM1* diagram. In the case of the specimen cr423c giving the API of 54.2 μT , $|\vec{k}'|$ of the NRM-TRM1* diagram is 0.126 and the degree of curvature in the NRM-TRM1 plot and the ARM0-ARM1 plot is not very consistent (Figure 5c).

Three specimens failed to give API estimates that met our criteria. Two of them (sc03f and sc03h) were from the CC category (Figures S5 and S6 in Supporting Information S1) while one of them (hw226a) was from the SS category. All of these were rejected as correlation coefficients in the NRM-TRM1* plots did not satisfy the criterion of $r_N \geq 0.995$. As for the specimen hw226a, the correlation coefficient in the TRM1-TRM2* plot was also out of the selection criterion of $r_T \geq 0.995$. It should be noted that remanence of the specimen hw226a was one to two orders of magnitude smaller than those of the other specimens.

3.2. MSP Method

The results from the MSP method shown in Figure 2 and Table 3 demonstrate that the “domain state correction” procedure suggested by Fabian and Leonhardt (2010) recovered the correct API value for none of the four categories. All were significantly underestimated.

Table 6
Same as in Table 5 but for Data of Tauxe et al. (2021)

Specimen	CAT	API	β	FRAC	g_{\max}	$ \vec{k}' $	SCAT	DANG	MAD
sc03h-CB3	CC	69.9	0.01	0.87	0.14	0.0693	True	2.22	3.89
sc03f-CA3	CC	67.2	0.02	0.87	0.13	0.1588	True	4.82	4.39
cr423c-CB5	CC	65.9	0.02	0.86	0.19	0.1559	True	1.49	4.36
sc03h-CB1	CC	72.8	0.02	0.80	0.16	0.1189	True	0.83	2.89
cr418f1-CA5	CC	65.0	0.03	0.85	0.22	0.1433	True	2.17	5.00
sc03h-CA3	CC	74.8	0.02	0.83	0.13	0.1383	True	4.23	4.98
sc03h-CA1	CC	77.5	0.02	0.93	0.12	0.1577	True	1.43	3.79
cr423c-CB1	CC	63.0	0.02	0.80	0.19	0.1451	True	5.03	3.49
sc03f-CB1	CC	71.7	0.02	0.80	0.15	0.1577	True	4.39	3.03
cr405g1-CA5	CS	70.6	0.02	0.98	0.11	0.1559	True	1.20	2.77
jm009i2-CB3	CS	69.4	0.01	0.81	0.13	0.1142	True	5.20	2.31
jm009d1-CB5	CS	69.4	0.01	0.94	0.12	0.1603	True	3.49	2.95
jm009c1-CB1	CS	69.4	0.02	0.79	0.27	0.1016	True	1.32	2.47
jm011d1-CB1	CS	69.5	0.02	0.89	0.16	0.1495	True	3.31	2.78
jm009i2-CA1	CS	69.5	0.02	0.84	0.12	0.1423	True	4.67	4.22
jm009f2-CB5	CS	69.5	0.02	0.85	0.30	0.1598	True	3.38	1.89
cr405g1-CB5	CS	69.5	0.01	0.81	0.11	0.0009	True	1.06	2.12
jm009i2-CB1	CS	69.5	0.01	0.91	0.12	0.1220	True	3.21	2.41
jm009d1-CB1	CS	71.9	0.02	0.83	0.14	0.1508	True	5.67	3.12
jm009i2-CA3	CS	69.6	0.01	0.83	0.14	0.1166	True	4.99	4.39
jm009f2-CB3	CS	69.6	0.02	0.91	0.30	0.1636	True	0.44	2.58
jm011d1-CA5	CS	69.3	0.02	0.92	0.17	0.1520	True	4.39	4.84
jm009c1-CB3	CS	69.6	0.01	0.93	0.22	0.1549	True	1.97	2.41
jm009f2-CA1	CS	69.7	0.02	0.80	0.29	0.1496	True	3.46	4.62
jm009d1-CA1	CS	69.7	0.01	0.84	0.13	0.1107	True	4.15	3.25
cr405g1-CA1	CS	70.7	0.01	0.82	0.11	0.0557	True	0.68	3.39
jm009d1-CA5	CS	69.6	0.01	0.78	0.16	0.0000	True	2.27	4.44
jm009f2-CA3	CS	69.5	0.01	0.80	0.29	0.1445	True	3.03	3.02
jm009c1-CA5	CS	68.9	0.02	0.93	0.23	0.1593	True	4.51	4.46
jm009f2-CB1	CS	65.4	0.02	0.86	0.29	0.1594	True	3.19	2.60
cr405g1-CB1	CS	66.4	0.01	0.87	0.10	0.0198	True	0.76	2.35
jm011d1-CA1	CS	66.9	0.02	0.79	0.20	0.1572	True	4.95	3.25
jm009i2-CB5	CS	67.0	0.02	0.85	0.14	0.1579	True	4.38	2.50
jm009d1-CA3	CS	77.2	0.01	0.81	0.14	0.0786	True	1.94	3.99
jm011d1-CB3	CS	68.1	0.01	0.95	0.16	0.1635	True	5.58	2.51
cr405g1-CB3	CS	67.0	0.01	0.87	0.10	0.0000	True	0.87	2.01
jm009c1-CB5	CS	68.5	0.01	0.96	0.24	0.1626	True	1.77	2.51
jm009d1-CB3	CS	76.0	0.01	0.81	0.14	0.0914	True	5.39	2.48
cr405g1-CA3	CS	66.3	0.01	0.86	0.11	0.0000	True	0.64	4.88
mc117e-SB5	SC	71.6	0.02	0.80	0.17	0.1092	True	1.86	3.90
mc117a-SA1	SC	64.7	0.02	0.79	0.19	0.1487	True	1.62	2.57
mc117d-SA3	SC	65.8	0.02	0.87	0.19	0.1588	True	1.86	3.36
mc117b-SB3	SC	71.1	0.02	0.79	0.24	0.1189	True	0.58	1.46

Table 6
Continued

Specimen	CAT	API	β	FRAC	g_{\max}	$ \vec{k}' $	SCAT	DANG	MAD
mc117e-SB3	SC	71.0	0.01	0.79	0.19	0.0969	True	1.56	2.75
mc117e-SA3	SC	71.5	0.02	0.80	0.16	0.1525	True	4.97	3.01
mc117e-SA5	SC	72.3	0.02	0.88	0.14	0.1599	True	1.87	2.60
mc117e-SB1	SC	72.7	0.02	0.87	0.16	0.1569	True	1.92	3.08
mc117b-SB5	SC	71.2	0.00	0.82	0.23	0.0002	True	1.42	1.91
mc117d-SA5	SC	73.2	0.02	0.88	0.19	0.1527	True	1.10	2.51
mc117b-SA5	SC	73.3	0.02	0.86	0.16	0.0000	True	0.05	2.81
mc117d-SB1	SC	71.0	0.01	0.85	0.24	0.0847	True	1.48	2.32
mc117a-SB3	SC	70.2	0.02	0.80	0.23	0.1488	True	1.30	3.80
mc117d-SB5	SC	69.0	0.02	0.78	0.20	0.0746	True	1.74	2.95
mc117a-SB5	SC	75.2	0.01	0.87	0.17	0.0982	True	1.54	2.60
mc117b-SB1	SC	68.8	0.02	0.94	0.15	0.1447	True	2.01	2.91
mc117e-SA1	SC	71.2	0.02	0.89	0.15	0.1474	True	2.47	2.98
mc117d-SB3	SC	73.5	0.02	0.83	0.18	0.1319	True	2.25	2.44
mc117a-SA5	SC	66.7	0.02	0.91	0.18	0.1562	True	1.67	2.93
mc117b-SA1	SC	67.4	0.02	0.82	0.20	0.1592	True	1.76	3.40
mc117a-SA3	SC	69.8	0.02	0.84	0.19	0.1625	True	2.90	3.70
mc117b-SA3	SC	73.9	0.02	0.80	0.18	0.1143	True	1.73	3.56
mc117d-SA1	SC	79.2	0.02	0.87	0.21	0.1391	True	0.29	2.32
mc117a-SB1	SC	71.2	0.01	0.86	0.18	0.0766	True	1.60	3.78
mc120b-SA3	SS	77.3	0.01	0.82	0.21	0.0000	True	1.05	4.85
mc120c-SB1	SS	76.8	0.01	0.79	0.16	0.0798	True	0.88	2.51
mc120b-SA5	SS	77.9	0.01	0.89	0.18	0.0370	True	1.88	3.81
mc120b-SA1	SS	75.3	0.01	0.80	0.19	0.0356	True	0.51	4.24
mc109d-SB3	SS	71.5	0.01	0.88	0.17	0.0466	True	2.52	2.77
mc120b-SB5	SS	73.0	0.01	0.79	0.22	0.0000	True	0.55	3.31
mc167d2-SB5	SS	72.0	0.01	0.90	0.21	0.0246	True	2.41	3.53
mc109e-SB1	SS	56.6	0.02	0.80	0.23	0.1619	True	1.79	4.72
hw226a-SA5	SS	71.1	0.03	0.79	0.20	0.1380	True	0.97	2.72
mc167d2-SA3	SS	61.7	0.01	0.87	0.20	0.0731	True	3.84	4.88
mc167d2-SA1	SS	64.1	0.02	0.97	0.25	0.1130	True	1.74	3.71
hw226a-SA3	SS	66.3	0.01	0.87	0.24	0.0416	True	1.68	1.37
mc120c-SB5	SS	67.4	0.01	0.87	0.18	0.0732	True	6.71	4.26
mc109d-SA5	SS	68.3	0.01	0.89	0.13	0.0878	True	1.77	4.87
mc167d2-SB3	SS	68.5	0.02	0.82	0.23	0.1066	True	2.89	2.41
mc120c-SA5	SS	68.6	0.01	0.79	0.14	0.0000	True	1.07	2.92
mc167d2-SB1	SS	68.9	0.01	0.83	0.22	0.0945	True	3.51	2.69
mc109e-SA1	SS	69.2	0.02	0.84	0.23	0.1437	True	4.09	2.75
mc167d2-SA5	SS	69.8	0.01	0.93	0.22	0.0288	True	2.19	1.89
hw226a-SA1	SS	71.3	0.02	0.81	0.22	0.0962	True	1.84	2.42
mc109d-SA3	SS	70.3	0.01	0.79	0.17	0.0505	True	3.13	4.01
mc120c-SB3	SS	70.9	0.01	0.79	0.17	0.0421	True	1.52	3.20
hw226a-SB3	SS	70.9	0.02	0.91	0.20	0.0000	True	1.38	1.30

Table 6
Continued

Specimen	CAT	API	β	FRAC	g_{\max}	$ \vec{k}' $	SCAT	DANG	MAD
hw226a-SB1	SS	70.9	0.01	0.80	0.21	0.0167	True	0.57	1.63
mc120c-SA1	SS	71.0	0.01	0.94	0.12	0.0886	True	1.59	3.90
mc109d-SA1	SS	71.0	0.01	0.97	0.13	0.0986	True	2.23	3.74
mc120b-SB1	SS	71.0	0.01	0.94	0.20	0.0473	True	1.58	3.13
mc109e-SA3	SS	71.0	0.01	0.92	0.15	0.1138	True	2.53	3.92
mc120c-SA3	SS	71.1	0.01	0.99	0.10	0.0427	True	2.34	3.91
mc109e-SB5	SS	71.1	0.01	0.88	0.15	0.0925	True	1.79	2.94
mc109e-SA5	SS	71.1	0.01	0.89	0.23	0.0915	True	4.29	2.35
mc109d-SB5	SS	70.7	0.02	0.86	0.16	0.1551	True	0.89	2.67
mc120b-SB3	SS	85.9	0.01	0.88	0.19	0.0810	True	1.32	3.52

3.3. AF-IZZI

We analyzed the data from the experiment in which specimens were treated with a 10 mT AF field prior to measurements. Arai plots for all experiments are shown in Figure 3 and the results using the CCRIT selection criteria (Cromwell et al., 2015; Tauxe et al., 2016) are listed in Table 4. Of the 38 specimens subjected to the AF-IZZI experiment, 25 passed the CCRIT specimen level criteria. These gave an average API of $73.7 \pm 3.3 \mu\text{T}$. The 12 SS specimens yielded an average of $72.6 \pm 3.0 \mu\text{T}$; the 7 SC specimens had a mean API of $76.6 \pm 3.4 \mu\text{T}$; the six CS specimens had an average of $71.8 \pm 1.8 \mu\text{T}$, but no CC specimens passed the CCRIT criteria. Apart from the SC specimens, CCRIT produced accurate results, but failed to improve the performance of the most curved (and likely coarsest grained) samples. In addition, the over-estimate of the SC specimens in those that passed CCRIT is worrisome. In fact, this type of behavior led to the adoption of site level consistency tests (Cromwell et al., 2015), a practice that improved agreement of site level estimates with the known historical fields in which the lavas cooled. In the case of our SC samples, all of the estimates were higher than the $70 \mu\text{T}$ lab field used for acquisitions of the fresh TRMs, and the data, if treated as a "site" would lead to an over-estimate of the API. Hence, we do not recommend using the AF-IZZI.

3.4. Reanalysis of Previously Published IZZI Results Using the CCRIT Criteria

We reanalyzed the data from the experiments of Santos and Tauxe (2019) and Tauxe et al. (2021) using the CCRIT selection criteria. These are listed in Tables 5 and 6, respectively, and shown in Figure 4. Eighteen of the 20 specimens analyzed passed CCRIT in the Santos and Tauxe (2019) study and 96 in the Tauxe et al. (2021) study. These had average APIs of $72.3 \pm 2.9 \mu\text{T}$ and $70.3 \pm 3.8 \mu\text{T}$, respectively. Figure 4 and Tables 5 and 6 show that experiments on the "fresh" TRMs conducted by Santos and Tauxe (2019) (ST19-CCRIT) and the experiments on the "aged" TRMs conducted by Tauxe et al. (2021) (T21-CCRIT) are within a few μT of the $70 \mu\text{T}$ field used for acquisitions of the fresh TRMs. This is achieved through the rejection of curved Arai plots and only using the "straight" results.

4. Discussion

4.1. Comparisons of the Results Between the TS Method and the IZZI Thellier Method

We compare the API estimates obtained by the TS method and those by the IZZI Thellier method using the CCRIT criteria on the aged sister specimens (Figure 6). Cumulative distributions of the two sets of APIs and their 95% bounds are shown in Figure 7. API estimates for the TS method range from 54.2 to 74.3 μT . Those from the aged IZZI experiments range from 56.6 to 85.9 μT . From the cumulative distributions shown in Figure 7, it appears possible that the IZZI method on the two-year-aged specimens allows more inaccurate estimates that are biased high. 95% of the values in the TS experiments are in the range of 64–74 μT while those in the aged IZZI experiments ranged from 63 to 79 μT (dotted bounds in Figure 7). However, there were many more specimens in the

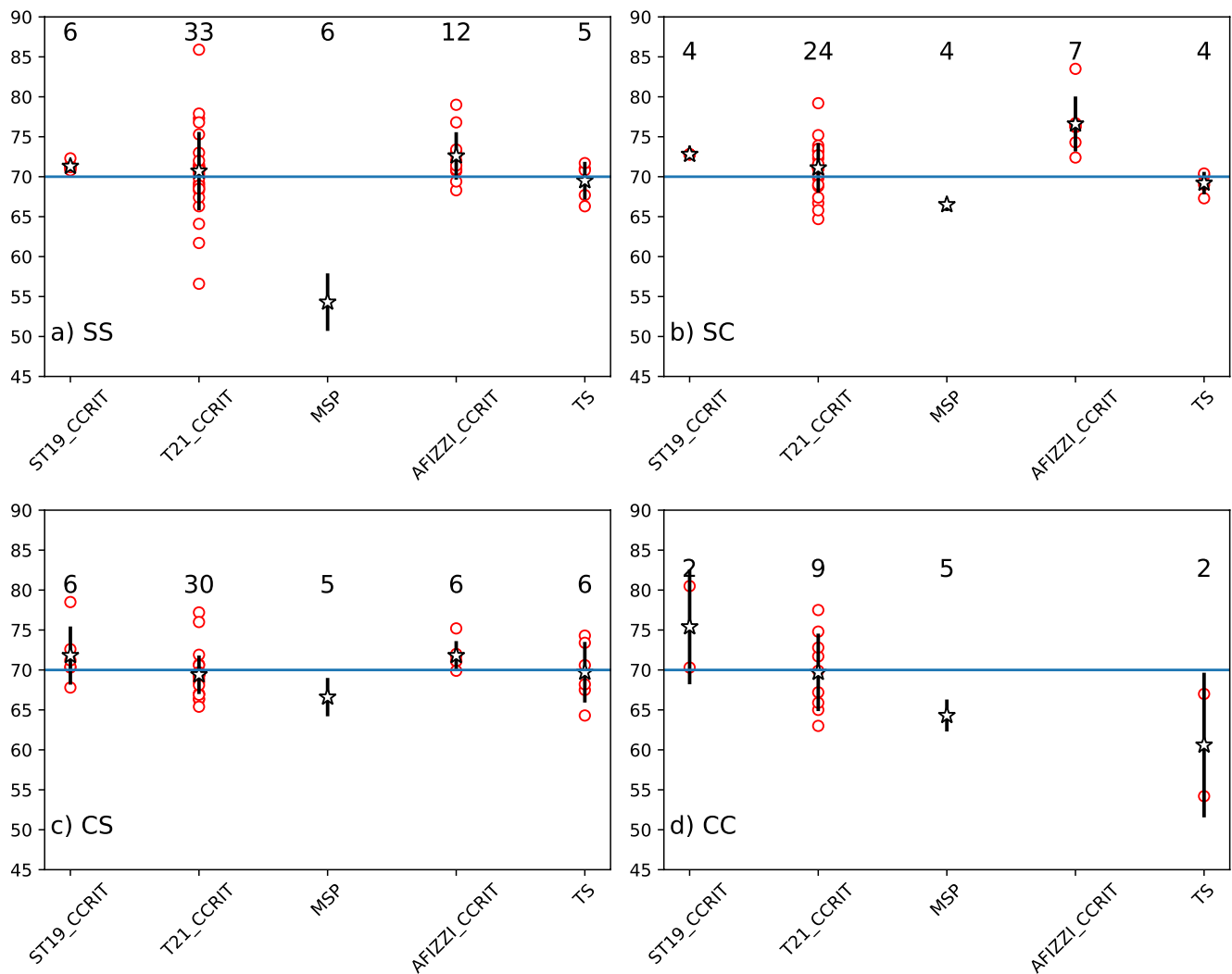


Figure 4. Summary of results of all experiments presented here, as well as the data from prior publications as reanalyzed here. Red dots are API estimates from individual specimens. Stars are the category means for each method. The black bars are the 1σ confidence bounds. Numbers above each method are the number of specimens used in each average. (a) straight-straight (SS) category, (b) straight-curved (SC) category, (c) curved-straight (CS) category, (d) curved-curved (CC) category.

aged IZZI collection and in fact the null hypothesis that the two distributions are similar cannot be rejected at the 95% level of confidence based on a Student's t -test p -value of 0.08. Agreement of APIs between the TS method and the IZZI Thellier method with the CCRIT has been previously demonstrated (Yamamoto & Yamaoka, 2018).

Both experimental protocols applied here eliminate chemical alteration as a cause for failure of the intensity experiments by choosing natural samples that did not appear to alter in the original experiments. Also, because the laboratory fields during the experiments were applied parallel to the initial TRMs in the IZZI Thellier experiment, anisotropy will not bias the results either (in the TS method, anisotropy correction has been built-in using ARMs). We can therefore evaluate what the best-case accuracy of API experiments can be. Regarding the data set generated by the TS method, 95% of them can have up to 6 μT bias. Using the largest data set we consider here, the experiments of Tauxe et al. (2021), we see that 95% of the data can have up to 9 μT bias. Taking all of the data without excluding "outliers," both methods can have a bias of up to 16 μT at the specimen level. This is far larger than the 6 μT estimate of uncertainty predicted by Paterson et al. (2012) based on laboratory sources of error alone.

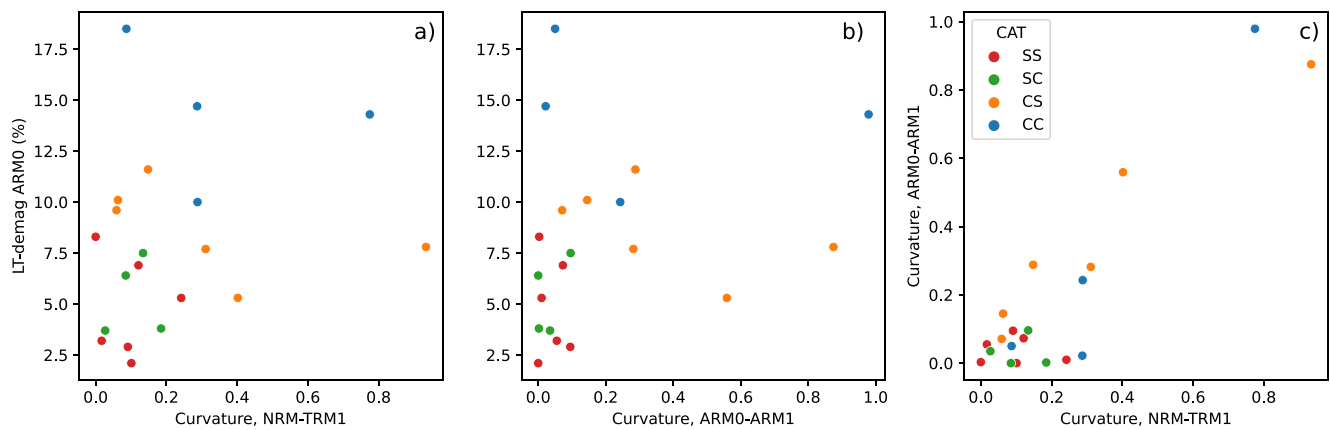


Figure 5. Comparison between low-temperature (LT)-demagnetized ARM0 fractions and curvatures (\bar{k}) in the NRM-TRM1 plots (a) and the ARM0-ARM1 plots (b). (c) Curvature of the NRM-TRM1 plots against curvature of the ARM0-ARM1 plots.

4.2. Rock Magnetic Parameters and API Estimates by the TS Method

A series of the rock magnetic parameters of the sister specimens from the same samples used in the present study were reported in Tauxe et al. (2021). The parameters are as follows: bulk domain stability (BDS, Paterson et al., 2017); ratio of the tFORC and remFORC (Zhao et al., 2017) integrated over FORC Zones 1 and 3, respectively (Trans/Rem); width of FORC distribution along the horizontal axis (Width); full-width half-maximum value of a vertical profile through the peak of the coercivity distribution in FORC diagram (FWHM); nucleation peak field (NPF); and annihilation peak field (APF). Here, we compared these parameters with the API estimates by the TS method and the curvatures in the NRM-TRM1 plots to consider whether or not there are any discernible relationships. These parameters, which could be utilized as measures of nonSD behaviors, did not show any discernible relationships with the API estimates by the TS method (Figure S7 in Supporting Information S1) as well as the curvatures in the NRM-TRM1 plots (Figure S8 in Supporting Information S1). This suggests that the API estimates by the TS method are not much influenced by nonSD behaviors characterized by these parameters as a result of a series of the improvements including LTD and ARM corrections in the TS method.

4.3. Implications for the Cause of Fragile Curvature in Paleointensity Plots

In the IZZI Thellier method, the resultant Arai plots showed variable curvatures (\bar{k} , hereafter called IZZI curvature) including the results from "original" TRMs (Cromwell, Constable, et al., 2013; Cromwell, Tauxe, et al., 2013; Cromwell et al., 2015; Lawrence et al., 2009; Sbarbori et al., 2009). Tauxe et al. (2021) argued that the IZZI curvatures can be "fragile," as they can increase during aging. They attributed this curvature to a growth over time of an inequality between blocking and unblocking temperature spectra. It is possible that such an inequality does not necessarily result in biased API estimates in the TS method, because they are obtained

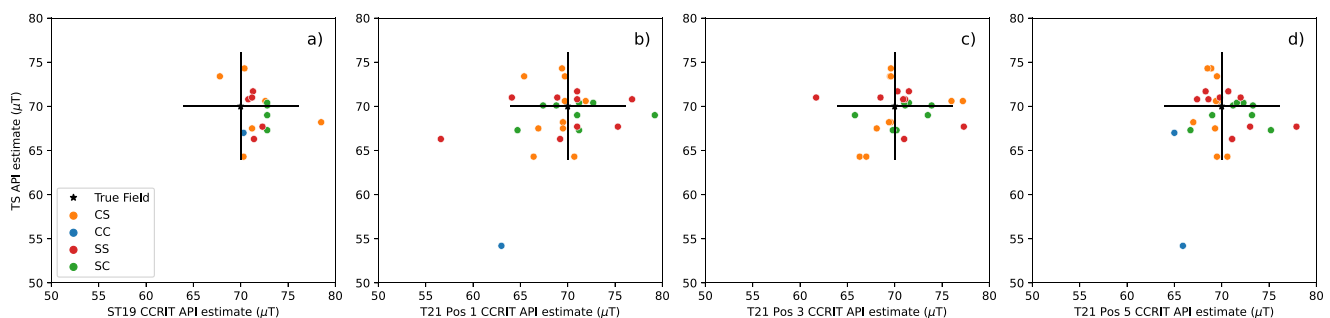


Figure 6. Comparisons of the absolute paleointensity (API) estimates by the Tsunakawa-Shaw (TS) method with those by the IZZI Thellier method using the CCRIT criteria for "fresh" thermoremanent magnetizations (TRMs) (a) and "aged" TRMs of positions 1, 3, and 5 (b–d), on the sister specimens. Black bars are the $\pm 6 \mu\text{T}$ bounds predicted by Paterson et al. (2012) for laboratory uncertainty in Thellier-type experiments.

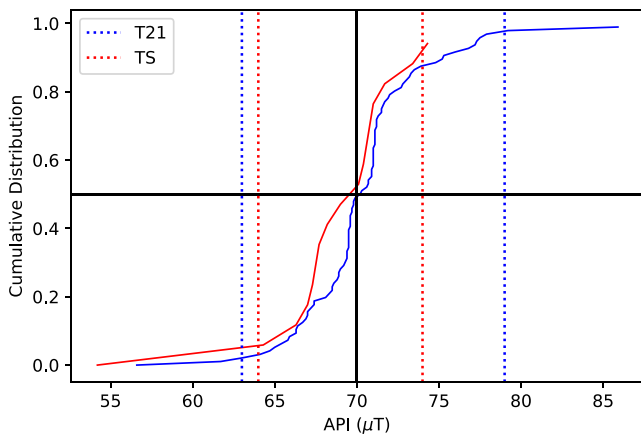


Figure 7. Cumulative distributions for the absolute paleointensity (API) estimates from the Tsunakawa-Shaw (TS) method (red) and the IZZI estimates reanalyzed from Tauxe et al. (2021) (blue) and the bounds containing 95% of the data in each group.

in coercivity space with a series of the improvements including LTD and ARM corrections (note that the CCRIT selection criteria accomplishes the same result in the IZZI Thellier experiments by rejecting specimens whose $|\vec{k}|$ values (evaluated over the fraction of remanence used $|\vec{k}'|$) exceed the threshold value of 0.164, as recommended by Paterson (2011)). When we think about relations of the IZZI curvatures to the API estimates by the TS method, reasonable estimates with $\sim 70 \mu\text{T}$ were obtained irrespective of the IZZI curvatures except for a single specimen in the CC category. Apart from that specimen, there is no tendency relating biased API estimates to samples with the larger IZZI curvatures (Figure 8).

Causes of the IZZI curvatures seem to be related to a remanence originating from the magnetocrystalline anisotropy, as there is a tendency that amounts of ARM0 demagnetized by LTD are larger for the samples with the larger IZZI curvatures (Figure 9). It is known that magnetocrystalline anisotropy constants of K_1 and K_2 show temperature dependences and the constants for Ti-poor titanomagnetites reach to zero at -130°C to -180°C (Syono & Ishikawa, 1963). These temperatures are achievable by liquid nitrogen (a boiling point of -196°C), and zero field cycling of a specimen between room temperature and liquid nitrogen temperature results in removal of a remanence originating from the magnetocrystalline anisotropies—this is a main concept of LTD.

It is thought that remanence carriers whose coercivities mainly originate from the magnetocrystalline anisotropies are probably susceptible for a time growth of inequality between blocking and unblocking temperature spectra resulting in the larger IZZI curvatures after aging, and such remanences can be removed by LTD. In light of this result, it would be interesting to incorporate the low temperature treatment into the IZZI experiment, as the incorporation of AF to 10 mT failed to improve the results. About the conventional Thellier experiment, inclusion of LTD has been attempted in several studies (e.g., Schmidt, 1993; Smirnov et al., 2017; Yamamoto et al., 2003).

The LTD treatment in the TS method did not always result in straight NRM-TRM1 and ARM0-ARM1 plots, although the degree of the curvature in the two plots are similar for the same specimens (Figure 5c) resulting in more or less straight NRM-TRM1* plots with reasonable API estimates, as stated in Section 3.1. There still seems to be causes of such curvatures in the TS method other than the remanence of magnetocrystalline anisotropy origin. One possible cause might be magnetostriction, which is known as a cause of coercivity. In the case of volcanic rocks, they are more or less quenched when they form. Magnetic minerals forming the rocks could be in a relatively high state of magnetostriction initially. As time passes under natural conditions, stress that causes the magnetostriction is thought to relax resulting in a lower state of magnetostriction. Another possible source is the possibility of multiple choices for the magnetization direction in grains other than the Néel particles (uniaxial single-domain) assumed by Thellier's requirements for successful API experiments (Thellier & Thellier, 1959). For example, the grain size range with surprisingly low stability owing to the preference for "hard-aligned" single vortex directions (Nagy et al., 2017) could result in changes in magnetization state during aging or during the

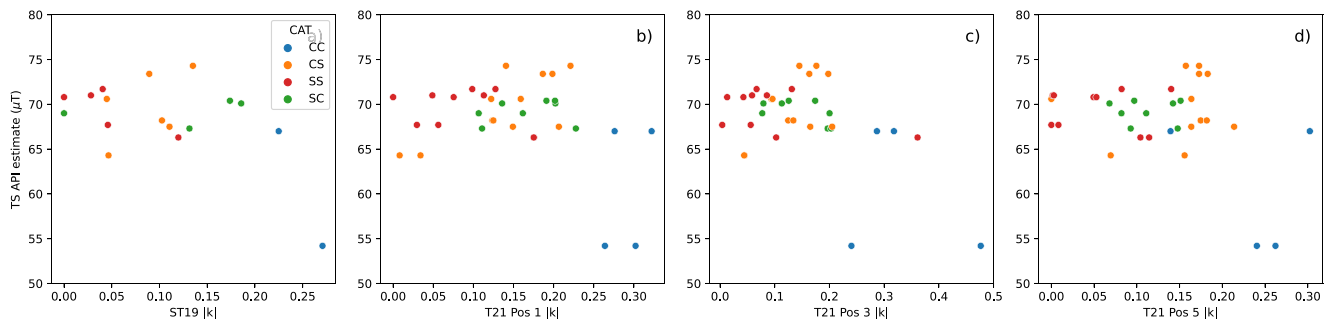


Figure 8. (a) Comparison between the absolute paleointensity (API) estimates by the TS method and the IZZI curvatures (\vec{k}) for "fresh" thermoremanent magnetizations (TRMs) and (b–d) "aged" TRMs of positions 1, 3, and 5.

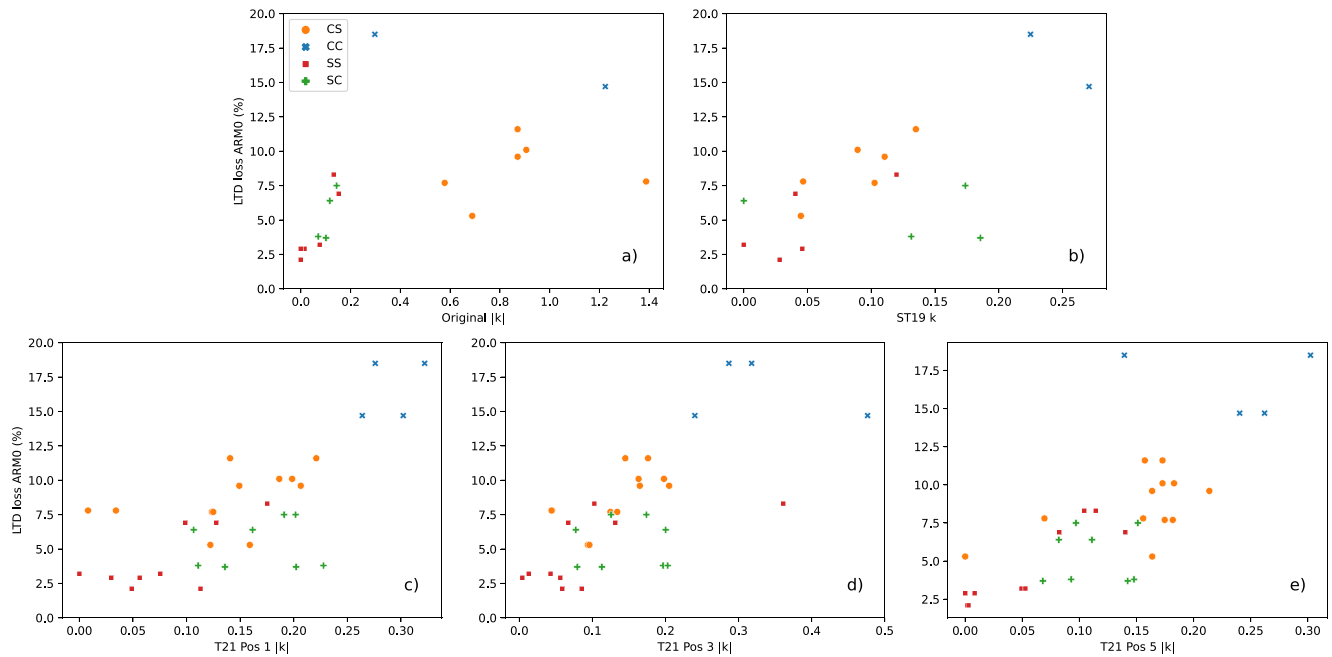


Figure 9. (a) Comparison between the low temperature (LT)-demagnetized ARM0 fraction in the TS method and the IZZI curvatures ($\left(\overline{|\vec{k}|}\right)$) for "original" TRMs, (b) "fresh" TRMs, and (c–e) "aged" TRMs of positions 1, 3, and 5.

paleointensity experiments themselves. Further exploration of this possibility will rely on extensive micromagnetic modeling research that is currently being actively pursued.

5. Conclusions

1. A total of 17 API estimates by the TS method were successfully obtained, resulting in an overall average (median) of 68.5 (69.0) μT with a standard deviation of 4.5 μT . This is indistinguishable from the laboratory field of 70 μT used for acquisitions of the fresh TRMs.
2. The MSP method performed poorly for all categories with a mean of $63 \pm 5 \mu\text{T}$.
3. The treatment with AF prior to measurement in the standard IZZI Thellier experimental protocol also performed poorly for several categories. None of the specimens in the coarsest grain size category (CC) passed our selection criteria and the category with bimodal grain sizes (SC) gave quite biased results ($76.6 \pm 3.4 \mu\text{T}$).
4. API estimates by the IZZI Thellier method previously obtained from sister specimens from the same samples used in the present study ("fresh" TRMs, Santos and Tauxe (2019); "aged" TRMs, Tauxe et al. (2021)) are reanalyzed using the CCRIT selection criteria. The results are within a few μT of the 70 μT field used for acquisitions of the fresh TRMs. When compared with the results by the TS method, both approaches yielded similar behavior and range of values, although the API range of the far larger data set of "aged" TRMs is somewhat larger than those from the TS method.
5. A series of the rock magnetic parameters of the sister specimens from the same samples used in the present study, which were reported in Tauxe et al. (2021) and could be utilized as measures of nonSD behaviors, did not show any discernible relationships with the API estimates by the TS method as well as the curvatures in the NRM-TRM1 plots. This suggests that the TS method excludes specimens influenced by nonSD behaviors as characterized by these parameters.
6. Remanence carriers whose coercivities mainly originate from magnetocrystalline anisotropy (thought to be associated with multidomain grains) or unstable magnetizations (thought to be associated from multiplicity of choice in magnetization directions (e.g., Nagy et al., 2017)) could be responsible for a growth of inequality between blocking and unblocking temperature spectra with aging, which has been suggested as a cause of the IZZI curvatures.

Data Availability Statement

Data generated for this paper are available at <https://earthref.org/MagIC/19509>. Previously published data are available in the MagIC database. The Python code developed to analyze results by the Tsunakawa-Shaw method is available in the PmagPy software package (<https://github.com/PmagPy/PmagPy>, see also: <https://earthref.org/PmagPy/cookbook>). The code can be executed without installation at <https://jupyterhub.earthref.org> after creating a personal account and running the PmagPy Online—Setup.ipynb Jupyter notebook and following instructions.

Acknowledgments

This work was supported by JSPS KAKENHI Grant Nos. 15H05832, 15K13564, 19KK0086, 20H00028, and 21H01171 to Y. Yamamoto, and NSF grants EAR1547263 and EAR1827263 to L. Tauxe. We thank Shinsuke Yagyū and Ken Matsumoto for assistance with the measurements. Constructive comments by Dr. Valera Shcherbakov and an anonymous reviewer improved the manuscript.

References

- Ahn, H., Kidane, T., Yamamoto, Y., & Otofujii, Y. (2016). Low geomagnetic field intensity in the Matuyama chron: Palaeomagnetic study of a lava sequence from Afar depression, east Africa. *Geophysical Journal International*, 204, 127–146. <https://doi.org/10.1093/gji/ggv303>
- Ahn, H., & Yamamoto, Y. (2019). Paleomagnetic study of basaltic rocks from Baengnyeong Island, Korea: Efficiency of the Tsunakawa–Shaw paleointensity determination on non-SD-bearing materials and implication for the early Pliocene geomagnetic field intensity. *Earth Planets and Space*, 71, 1–20. <https://doi.org/10.1186/s40623-019-1107-6>
- Cromwell, G., Constable, C., Staudigel, H., Tauxe, L., & Gans, P. (2013). Revised and updated paleomagnetic results from Costa Rica. *Geochemistry, Geophysics, Geosystems*, 14, 3379–3388. <https://doi.org/10.1002/ggge.20199>
- Cromwell, G., Tauxe, L., Staudigel, H., Constable, C., Koppers, A., & Pedersen, R.-B. (2013). In search of long-term hemispheric asymmetry in the geomagnetic field: Results from high northern latitudes. *Geochemistry, Geophysics, Geosystems*, 14, 3234–3249. <https://doi.org/10.1002/ggge.20174>
- Cromwell, G., Tauxe, L., Staudigel, H., & Ron, H. (2015). Paleointensity estimates from historic and modern Hawaiian lava flows using glassy basalt as a primary source material. *Physics of the Earth and Planetary Interiors*, 241, 44–56. <https://doi.org/10.1016/j.pepi.2014.12.007>
- Dekkers, M., & Böhm, H. (2006). Reliable absolute paleointensities independent of magnetic domain state. *Earth and Planetary Science Letters*, 248, 508–517. <https://doi.org/10.1016/j.epsl.2006.05.040>
- Dunlop, D., & Özdemir, O. (2001). Beyond Néel's theories: Thermal demagnetization of narrow-band partial thermoremanent magnetizations. *Physics of the Earth and Planetary Interiors*, 126, 43–57. [https://doi.org/10.1016/s0031-9201\(01\)00243-6](https://doi.org/10.1016/s0031-9201(01)00243-6)
- Dunlop, D., Zhang, B., & Özdemir, O. (2005). Linear and nonlinear Thellier paleointensity behavior of natural minerals. *Journal of Geophysical Research*, 110, B01103. <https://doi.org/10.1029/2004JB003095>
- Fabian, K., & Leonhardt, R. (2010). Multiple-specimen absolute paleointensity determination: An optimal protocol including pTRM normalization, domain-state correction, and alteration test. *Earth and Planetary Science Letters*, 297, 84–94. <https://doi.org/10.1016/j.epsl.2010.06.006>
- Heider, F., Dunlop, D., & Soffel, H. (1992). Low-temperature and alternating field demagnetization of saturation remanence and thermoremanence in magnetite grains (0.037 μm to 5 mm). *Journal of Geophysical Research*, 97, 9371–9381. <https://doi.org/10.1029/91jb03097>
- Hoffman, K. A., Constantine, V. L., & Morse, D. L. (1989). Determination of absolute palaeointensity using a multi-specimen procedure. *Nature*, 339, 295–297. <https://doi.org/10.1038/339295a0>
- Kato, C., Sato, M., Yamamoto, Y., Tsunakawa, H., & Kirschvink, J. (2018). Paleomagnetic studies on single crystals separated from the middle cretaceous iritono granite. *Earth Planets and Space*, 70, 176. <https://doi.org/10.1186/s40623-018-0945-y>
- Kitahara, Y., Nishiyama, D., Ohno, M., Yamamoto, Y., Kuwahara, Y., & Hatakeyama, T. (2021). Construction of new archaeointensity reference curve for East Asia from 200 CE to 1100 CE. *Physics of the Earth and Planetary Interiors*, 310, 106596. <https://doi.org/10.1016/j.pepi.2020.106596>
- Kitahara, Y., Yamamoto, Y., Ohno, M., Kuwahara, Y., Kameda, S., & Hatakeyama, T. (2018). Archeointensity estimates of a tenth-century kiln: First application of the Tsunakawa–Shaw paleointensity method to archeological relics. *Earth Planets and Space*, 70, 79. <https://doi.org/10.1186/s40623-018-0841-5>
- Krásá, D., Heunemann, C., Leonhardt, R., & Petersen, N. (2003). Experimental procedure to detect multidomain remanence during Thellier–Thellier experiments. *Physics and Chemistry of the Earth*, 28, 681–687. [https://doi.org/10.1016/S1474-7065\(03\)00122-0](https://doi.org/10.1016/S1474-7065(03)00122-0)
- Lawrence, K. P., Tauxe, L., Staudigel, H., Constable, C., Koppers, A., McIntosh, W. C., & Johnson, C. L. (2009). Paleomagnetic field properties at high southern latitude. *Geochemistry, Geophysics, Geosystems*, 10, Q01005. <https://doi.org/10.1029/2008GC002072>
- Levi, S. (1977). The effect of magnetite particle size on paleointensity determinations of the geomagnetic field. *Physics of the Earth and Planetary Interiors*, 13, 245–259. [https://doi.org/10.1016/0031-9201\(77\)90107-8](https://doi.org/10.1016/0031-9201(77)90107-8)
- Lloyd, S., Biggin, A., Halls, H., & Hill, M. (2021). First palaeointensity data from the cryogenian and their potential implications for inner core nucleation age. *Geophysical Journal International*, 226(1), 66–77. <https://doi.org/10.1093/gji/ggab090>
- Lloyd, S., Paterson, G., Thallner, D., & Biggin, A. (2021). Improvements to the Shaw-type absolute palaeointensity method. *Frontiers of Earth Science*, 9, 701863. <https://doi.org/10.3389/feart.2021.701863>
- Mochizuki, N., Fujii, S., Hasegawa, T., Yamamoto, Y., Hatakeyama, T., Yamashita, D., et al. (2021). A tephra-based approach to calibrating relative geomagnetic paleointensity stacks to absolute values. *Earth and Planetary Science Letters*, 572, 117119. <https://doi.org/10.1016/j.epsl.2021.117119>
- Mochizuki, N., Maruuchi, T., Yamamoto, Y., & Shibuya, H. (2013). Multi-level consistency tests in paleointensity determinations from the welded tuffs of the Aso pyroclastic-flow deposits. *Physics of the Earth and Planetary Interiors*, 223, 40–54. <https://doi.org/10.1016/j.pepi.2013.05.001>
- Mochizuki, N., Oda, H., Ishizuka, O., Yamazaki, T., & Tsunakawa, H. (2011). Paleointensity variation across the Matuyama–Brunhes polarity transition: Observations from lavas at Punaru Valley, Tahiti. *Journal of Geophysical Research*, 116. <https://doi.org/10.1029/2010JB008093>
- Mochizuki, N., Tsunakawa, H., Oishi, Y., Wakai, S., Wakabayashi, K., & Yamamoto, Y. (2004). Palaeointensity study of the Oshima 1986 lava in Japan: Implications for the reliability of the Thellier and LTD-DHT Shaw methods. *Physics of the Earth and Planetary Interiors*, 146, 395–416. <https://doi.org/10.1016/j.pepi.2004.02.007>
- Mochizuki, N., Tsunakawa, H., Shibuya, H., Cassidy, J., & Smith, I. (2006). Palaeointensities of the Auckland geomagnetic excursions by the LTD-DHT Shaw method. *Physics of the Earth and Planetary Interiors*, 154, 168–179. <https://doi.org/10.1016/j.pepi.2005.09.005>
- Nagata, T., Arai, Y., & Momose, K. (1963). Secular variation of the geomagnetic total force during the last 5000 years. *Journal of Geophysical Research*, 68, 5277–5281. <https://doi.org/10.1029/j.2156-2202.1963.tb00005.x>

- Nagy, L., Williams, W., Muxworthy, A., Fabian, K., Almeida, T., Conbhuui, P., & Shcherbakov, V. (2017). Stability of equidimensional pseudo-single-domain magnetite over billion-year timescales. *Proceedings of the National Academy of Sciences*, *114*, 10356–10360. <https://doi.org/10.1073/pnas.1708344114>
- Oishi, Y., Tsunakawa, H., Mochizuki, N., Yamamoto, Y., Wakabayashi, K., & Shibuya, H. (2005). Validity of the LTD-DHT Shaw and Thellier paleointensity methods: A case study of the Kilauea 1970 lava. *Physics of the Earth and Planetary Interiors*, *149*, 243–257. <https://doi.org/10.1016/j.pepi.2004.10.009>
- Okayama, K., Mochizuki, N., Wada, Y., & Otofujii, Y. (2019). Low absolute paleointensity during Late Miocene excursion of the Earth's magnetic field. *Physics of the Earth and Planetary Interiors*, *287*, 10–20. <https://doi.org/10.1016/j.pepi.2018.12.006>
- Ozima, M., Ozima, M., & Akimoto, S. (1964). Low temperature characteristics of remanent magnetization of magnetite. *Journal of Geomagnetism and Geoelectricity*, *16*, 165–177. <https://doi.org/10.5636/jgg.16.165>
- Paterson, G. (2011). A simple test for the presence of multidomain behavior during paleointensity experiments. *Journal of Geophysical Research*, *116*(B10). <https://doi.org/10.1029/2011JB008369>
- Paterson, G., Biggin, A., Yamamoto, Y., & Pan, Y. (2012). Towards the robust selection of Thellier-type paleointensity data: The influence of experimental noise. *Geochemistry, Geophysics, Geosystems*, *13*(5). <https://doi.org/10.1029/2012GC004046>
- Paterson, G., Muxworthy, A., Yamamoto, Y., & Pan, Y. (2017). Bulk magnetic domain stability controls paleointensity fidelity. *Proceedings of the National Academy of Sciences*, *114*, 13120–13125. <https://doi.org/10.1073/pnas.1714047114>
- Paterson, G., Tauxe, L., Biggin, A., Shaar, R., & Jonestrask, L. (2014). On improving the selection of Thellier-type paleointensity data. *Geochemistry, Geophysics, Geosystems*, *15*, 1180–1192. <https://doi.org/10.1002/2013GC005135>
- Pike, C., Roberts, A., & Verosub, K. (1999). Characterizing interactions in fine magnetic particle systems using first order reversal curves. *Journal of Applied Physics*, *85*, 6660–6667. <https://doi.org/10.1063/1.370176>
- Rolph, T. C., & Shaw, J. (1985). A new method of palaeofield magnitude correction for thermally altered samples and its application to Lower Carboniferous lavas. *Geophysical Journal of the Royal Astronomical Society*, *80*, 773–781. <https://doi.org/10.1111/j.1365-246x.1985.tb05124.x>
- Santos, C., & Tauxe, L. (2019). Investigating the accuracy, precision, and cooling rate dependence of laboratory-acquired thermal remanences during paleointensity experiments. *Geochemistry, Geophysics, Geosystems*, *20*, 383–397. <https://doi.org/10.1029/2018GC007946>
- Sbarbori, E., Tauxe, L., Goguitaichvili, A., Urrutia-Fucugauchi, J., & Bohron, W. (2009). Paleomagnetic behavior of volcanic rocks from Isla Socorro, Mexico. *Earth Planets and Space*, *61*, 191–204. <https://doi.org/10.1186/BF03352899>
- Schmidt, P. W. (1993). Palaeomagnetic cleaning strategies. *Physics of the Earth and Planetary Interiors*, *76*, 169–178. [https://doi.org/10.1016/0031-9201\(93\)90066-i](https://doi.org/10.1016/0031-9201(93)90066-i)
- Shaar, R., & Tauxe, L. (2013). Thellier GUI: An integrated tool for analyzing paleointensity data from Thellier-type experiments. *Geochemistry, Geophysics, Geosystems*, *14*, 677–692. <https://doi.org/10.1002/ggge.20062>
- Shaar, R., & Tauxe, L. (2015). Instability of thermoremanence and the problem of estimating the ancient geomagnetic field strength from non-single-domain recorders. *Proceedings of the National Academy of Sciences*, *112*, 11187–11192. <https://doi.org/10.1073/pnas.1507986112>
- Shaw, J. (1974). A new method of determining the magnitude of the paleomagnetic field: Application to five historic lavas and five archeological samples. *Geophysical Journal of the Royal Astronomical Society*, *39*, 133–141. <https://doi.org/10.1111/j.1365-246x.1974.tb05443.x>
- Singer, B., Jicha, B., Mochizuki, N., & Coe, R. (2019). Synchronizing volcanic, sedimentary, and ice core records of earth's last magnetic polarity reversal. *Science Advances*, *5*, eaaw4621. <https://doi.org/10.1126/sciadv.aaw4621>
- Smirnov, A., Kulakov, E., Foucher, M., & Bristol, K. (2017). Intrinsic paleointensity bias and the long-term history of the geodynamo. *Science Advances*, *3*, e1602306. <https://doi.org/10.1126/sciadv.1602306>
- Syono, Y., & Ishikawa, Y. (1963). Magnetocrystalline anisotropy of $x\text{Fe}_2\text{TiO}_4(1-x)\text{Fe}_3\text{O}_4$. *Journal of the Physical Society of Japan*, *18*(8), 1230–1231. <https://doi.org/10.1143/jpsj.18.1230>
- Tauxe, L., Santos, C., Cych, B., Zhao, X., Roberts, A., Nagy, L., & Williams, W. (2021). Understanding non-ideal paleointensity recording in igneous rocks: Insights from aging experiments on lava samples and the causes and consequences of "fragile" curvature in Arai plots. *Geochemistry, Geophysics, Geosystems*, *22*, e2020GC009423. <https://doi.org/10.1029/2020GC009423>
- Tauxe, L., Shaar, R., Jonestrask, L., Swanson-Hysell, N., Minnett, R., Koppers, A. A. P., et al. (2016). Pmagpy: Software package for paleomagnetic data analysis and a bridge to the Magnetics Information Consortium (MagIC) Database. *Geochemistry, Geophysics, Geosystems*, *17*, 2450–2463. <https://doi.org/10.1002/2016GC006307>
- Thallner, D., Biggin, A., & Halls, H. (2021). An extended period of extremely weak geomagnetic field suggested by paleointensities from the Ediacaran Grenville dykes (SE Canada). *Earth and Planetary Science Letters*, *568*, 117025. <https://doi.org/10.1016/j.epsl.2021.117025>
- Thallner, D., Biggin, A., McCausland, P., & Fu, R. (2021). New paleointensities from the Skinner Cove Formation, Newfoundland, suggest a changing state of the geomagnetic field at the Ediacaran-Cambrian transition. *Journal of Geophysical Research: Solid Earth*, *126*, e2021JB022292. <https://doi.org/10.1029/2021JB022292>
- Thellier, E., & Thellier, O. (1959). Sur l'intensité du champ magnétique terrestre dans le passé historique et géologique. *Annales Geophysicae*, *15*, 285–378.
- Tsunakawa, H., & Shaw, J. (1994). The Shaw method of paleointensity determinations and its application to recent volcanic rocks. *Geophysical Journal International*, *118*, 781–787. <https://doi.org/10.1111/j.1365-246x.1994.tb03999.x>
- Tsunakawa, H., Wakabayashi, K., Mochizuki, N., Yamamoto, Y., Ishizaka, K., Hirata, T., et al. (2009). Paleointensity study of the middle Cretaceous Iritono granite in northeast Japan: Implication for high field intensity of the Cretaceous normal superchron. *Physics of the Earth and Planetary Interiors*, *176*(3–4), 235–242. <https://doi.org/10.1016/j.pepi.2009.07.001>
- Yamamoto, Y., & Hoshi, H. (2008). Paleomagnetic and rock magnetic studies of the Sakurajima 1914 and 1946 andesitic lavas from Japan: A comparison of the LTD-DHT Shaw and Thellier paleointensity methods. *Physics of the Earth and Planetary Interiors*, *167*, 118–143. <https://doi.org/10.1016/j.pepi.2008.03.006>
- Yamamoto, Y., Ishizuka, O., Sudo, M., & Uto, K. (2007). $^{40}\text{Ar}/^{39}\text{Ar}$ ages and paleomagnetism of transitionally magnetized volcanic rocks in the Society Islands, French Polynesia: Raiatea excursion in the upper-Gauss chron. *Geophysical Journal International*, *169*, 41–59. <https://doi.org/10.1111/j.1365-246x.2006.03277.x>
- Yamamoto, Y., & Shaw, J. (2008). Development of the microwave LTD-DHT Shaw method for absolute paleointensity determination. *Physics of the Earth and Planetary Interiors*, *170*, 15–23. <https://doi.org/10.1016/j.pepi.2008.06.021>
- Yamamoto, Y., Torii, M., & Natsuhara, N. (2015). Archeointensity study on baked clay samples taken from the reconstructed ancient kiln: Implication for validity of the Tsunakawa-Shaw paleointensity method. *Earth Planets and Space*, *67*, 63. <https://doi.org/10.1186/s40623-015-0229-8>
- Yamamoto, Y., & Tsunakawa, H. (2005). Geomagnetic field intensity during the last 5 Myr: LTD-DHT Shaw paleointensities from volcanic rocks of the Society Islands, French Polynesia. *Geophysical Journal International*, *162*(1), 79–114. <https://doi.org/10.1111/j.1365-246x.2005.02651.x>

- Yamamoto, Y., Tsunakawa, H., Shaw, J., & Kono, M. (2007). Paleomagnetism of the Datong monogenetic volcanoes in China: Paleodirection and paleointensity during the middle to early Brunhes Chron. *Earth Planets and Space*, *59*, 727–746. <https://doi.org/10.1186/bf03352736>
- Yamamoto, Y., Tsunakawa, H., & Shibuya, H. (2003). Palaeointensity study of the Hawaiian 1960 lava: Implications for possible causes of erroneously high intensities. *Geophysical Journal International*, *153*(1), 263–276. <https://doi.org/10.1046/j.1365-246x.2003.01909.x>
- Yamamoto, Y., & Yamaoka, R. (2018). Paleointensity study on the Holocene surface lavas on the Island of Hawaii using the Tsunakawa-Shaw method. *Frontiers of Earth Science*, *6*, 48. <https://doi.org/10.3389/feart.2018.00048>
- Yamazaki, T., & Yamamoto, Y. (2014). Paleointensity of the geomagnetic field in the Late Cretaceous and earliest paleogene obtained from drill cores of the Louisville seamount trail. *Geochemistry, Geophysics, Geosystems*, *15*, 2454–2466. <https://doi.org/10.1002/2014GC005298>
- Yamamoto, Y., Shibuya, H., Tanaka, H., & Hoshizumi, H. (2010). Geomagnetic paleointensity deduced for the last 300 kyr from Unzen Volcano, Japan, and the dipolar nature of the Iceland Basin excursion. *Earth and Planetary Science Letters*, *293*, 236–249. <https://doi.org/10.1016/j.epsl.2010.02.024>
- Yoshimura, Y., Yamazaki, T., Yamamoto, Y., Ahn, H., Kidane, T., & Otofujii, Y. (2020). Geomagnetic paleointensity around 30 Ma estimated from Afro-Arabian Large Igneous Province. *Geochemistry, Geophysics, Geosystems*, *21*, e2020GC009341. <https://doi.org/10.1029/2020gc009341>
- Yu, Y., Tauxe, L., & Genevey, A. (2004). Toward an optimal geomagnetic field intensity determination technique. *Geochemistry, Geophysics, Geosystems*, *5*(2), Q02H07. <https://doi.org/10.1029/2003GC000630>
- Zhao, X., Roberts, A., Heslop, D., Paterson, G., Li, Y., & Li, J. (2017). Magnetic domain state diagnosis using hysteresis reversal curves. *Journal of Geophysical Research*, *122*, 4767–4789. <https://doi.org/10.1002/2016JB013683>